NAVAL POSTGRADUATE SCHOOL

MONTEREY, CALIFORNIA

THESIS

SIMULATING HEL LETHALITY WITH COMPLEX CAD GEOMETRIES

by

Alex J. Shelander

June 2023

Thesis Advisor: Dragoslav Grbovic
Co-Advisors: Joseph A. Blau
Keith R. Cohn

THIS PAGE INTENTIONALLY LEFT BLANK

REPORT DOCUMENTATION PAGE	*Form Approved OMB No. 0704-0188*

1. AGENCY USE ONLY *(Leave blank)*	**2. REPORT DATE** June 2023	**3. REPORT TYPE AND DATES COVERED** Master's thesis

4. TITLE AND SUBTITLE SIMULATING HEL LETHALITY WITH COMPLEX CAD GEOMETRIES	**5. FUNDING NUMBERS** RPL24
6. AUTHOR(S) Alex J. Shelander	
7. PERFORMING ORGANIZATION NAME(S) AND ADDRESS(ES) Naval Postgraduate School Monterey, CA 93943-5000	**8. PERFORMING ORGANIZATION REPORT NUMBER**
9. SPONSORING / MONITORING AGENCY NAME(S) AND ADDRESS(ES) Office of Naval Research	**10. SPONSORING / MONITORING AGENCY REPORT NUMBER**

11. SUPPLEMENTARY NOTES The views expressed in this thesis are those of the author and do not reflect the official policy or position of the Department of Defense or the U.S. Government.

12a. DISTRIBUTION / AVAILABILITY STATEMENT Approved for public release. Distribution is unlimited.	**12b. DISTRIBUTION CODE** A

13. ABSTRACT (maximum 200 words)

The US Navy has initialized research and development of shipborne high energy lasers (HEL) to counter anti-ship cruise missiles (ASCM) at terminal ranges. The previous modeling method for HEL lethality in COMSOL could not model complex geometry, preventing proper planning against such threats. Evolving from a two-dimensional to a three-dimensional environment required additional studies in error tolerances, accurate melt velocities, and meshing methods—ultimately enabling the use of computer-aided design (CAD) models. Using such models will allow accurate analysis of HEL lethality against specific threats, resulting in proper tactics and firing doctrine to ensure the ship's defense.

14. SUBJECT TERMS direct, energy, defense, high energy laser, HEL, anti-ship cruise missile, ASCM, computer-generated design, CAD, COMSOL	**15. NUMBER OF PAGES** 85
	16. PRICE CODE

17. SECURITY CLASSIFICATION OF REPORT Unclassified	**18. SECURITY CLASSIFICATION OF THIS PAGE** Unclassified	**19. SECURITY CLASSIFICATION OF ABSTRACT** Unclassified	**20. LIMITATION OF ABSTRACT** UU

NSN 7540-01-280-5500

Standard Form 298 (Rev. 2-89)
Prescribed by ANSI Std. 239-18

THIS PAGE INTENTIONALLY LEFT BLANK

Approved for public release. Distribution is unlimited.

SIMULATING HEL LETHALITY WITH COMPLEX CAD GEOMETRIES

Alex J. Shelander
Lieutenant, United States Navy
BSEE, University of North Carolina, Charlotte, 2017
BS, University of North Carolina, Charlotte, 2017

Submitted in partial fulfillment of the
requirements for the degree of

MASTER OF SCIENCE IN APPLIED PHYSICS

from the

NAVAL POSTGRADUATE SCHOOL
June 2023

Approved by: Dragoslav Grbovic
Advisor

Joseph A. Blau
Co-Advisor

Keith R. Cohn
Co-Advisor

Frank A. Narducci
Chair, Department of Physics

THIS PAGE INTENTIONALLY LEFT BLANK

ABSTRACT

The US Navy has initialized research and development of shipborne high energy lasers (HEL) to counter anti-ship cruise missiles (ASCM) at terminal ranges. The previous modeling method for HEL lethality in COMSOL could not model complex geometry, preventing proper planning against such threats. Evolving from a two-dimensional to a three-dimensional environment required additional studies in error tolerances, accurate melt velocities, and meshing methods—ultimately enabling the use of computer-aided design (CAD) models. Using such models will allow accurate analysis of HEL lethality against specific threats, resulting in proper tactics and firing doctrine to ensure the ship's defense.

THIS PAGE INTENTIONALLY LEFT BLANK

Table of Contents

1 Introduction **1**

1.1 Area of Research 2

1.2 Research Objectives 4

1.3 Thesis Organization 4

2 Background **7**

2.1 Motivation for Directed Energy 8

2.2 Navy Directed Energy Programs 12

2.3 Propagation Effects and Challenges 18

3 Damage Effects of Directed Energy **25**

3.1 Targeting 25

3.2 Laser-Induced Heating and Heat Transfer in Metals 27

3.3 Damage by Melting 30

4 Model Setup and Methodology **35**

4.1 Assumptions and Scope 35

4.2 Governing Equations 36

4.3 Evolution from Flat Plate 40

4.4 Meshing Analysis 43

4.5 Ramped Coefficient Analysis 51

4.6 Error Tolerance Analysis 55

4.7 CAD Example 60

5 Conclusion **65**

5.1 Melting Method 65

5.2 Future Work 66

List of References **67**

Initial Distribution List **69**

THIS PAGE INTENTIONALLY LEFT BLANK

List of Figures

Figure 1.1 NPS Directed Energy Modeling Organizational Chart. Source: [1]. 3

Figure 2.1 Figure B: Office of Naval Research's Incremental Approach to Laser Weapon Development and Installation. Source: [2]. 12

Figure 2.2 SSL-TM Loadout and Configuration. Source: [2]. 14

Figure 2.3 ODIN System Installed on USS Stockdale (DDG 106). Source: [2]. 15

Figure 2.4 HELIOS Location and Beam Director, as Installed on a Flight IIA *Arleigh Burke*-Class Destroyer. Source: [3]. 16

Figure 2.5 DDG-X Concept and Layout. Source: [4]. 17

Figure 2.6 Absorption and Scattering Windows as a Function of Wavelength. Source: [5]. 18

Figure 2.7 Cross-Section of Beam Profile as a Function of Distance. Source: [5]. 22

Figure 3.1 DJI Phantom Pro V2. Source: [6]. 26

Figure 4.1 Heat Transfer Coefficient vs. Temperature for $\Gamma = 3 * 10^5$ 38

Figure 4.2 Three-Dimensional Flat Plate in COMSOL 41

Figure 4.3 Three-Dimensional Curved Plate in COMSOL, 300mm Radius of Curvature 42

Figure 4.4 Time to Melt through Plates of Various Radii of Curvature over Thicknesses Ranging from 0.1mm to 10mm 43

Figure 4.5 Displacement over Time for a 300mm Radius of Curvature Curved Plate and a 300mm Radius Full Cylinder for Various Thicknesses from 1mm to 5mm 44

Figure 4.6 Time to Melt through Plates and Cylinders of Various Radii of Curvature over Thicknesses Ranging from 0.1mm to 10mm 45

Figure 4.7 Method 1, Free Triangular Mesh 46
Figure 4.8 Method 2, Free Quad Mesh 47
Figure 4.9 Method 3, Free Tetrahedral Mesh 48
Figure 4.10 Time to Melt using Various Meshing Methods 49
Figure 4.11 Mapped Meshing Method 51
Figure 4.12 Displacement vs. Time for Mapped Mesh on a Curved Disc with Radius of 15cm and a Radius of Curvature of 300mm 52
Figure 4.13 Displacement vs. Time for Mapped Mesh on a Curved Disc with Radius of 19cm and a Radius of Curvature of 300mm 53
Figure 4.14 Displacement vs. Time for Mapped Mesh on a Curved Disc with Radius of 29 cm and a Radius of Curvature of 300mm 54
Figure 4.15 Displacement vs. Time of Various Ramped Coefficients for Mapped Mesh of 175 Elements across and 2 Thick on a Curved Disc with a Radius of 17 cm and a Radius of Curvature of 300mm for a 50 KW Beam over a 5cm Spot Si e 55
Figure 4.16 Displacement vs. Time of Various Ramped Coefficients for Mapped Mesh of 175 Elements across and 2 Thick on a Curved Disc with a Radius of 17 cm and a Radius of Curvature of 300mm for a 100 KW Beam over a 5cm Spot Size 56
Figure 4.17 Displacement vs. Time of Various Ramped Coefficients for Mapped Mesh of 175 Elements across and 2 Thick on a Curved Disc with a Radius of 17 cm and a Radius of Curvature of 300mm for a 200 KW Beam over a 5cm Spot Size 57
Figure 4.18 Displacement vs. Time of Various Radii for Error Tolerance of 0.1 58
Figure 4.19 Displacement vs. Time of Various Radii for Error Tolerance of 0.001 59
Figure 4.20 Displacement vs. Time of Various Ramped Coefficients for Error Tolerance of 1E-3 60
Figure 4.21 Displacement vs. Time of Various Ramped Coefficients for Error Tolerance of 1E-6 61
Figure 4.22 AE: Displacement vs. Time of Various Geometries 62

Figure 4.23 Heat and Displacement Profile of Lased Missile 63

THIS PAGE INTENTIONALLY LEFT BLANK

List of Tables

Table 3.1 Example Material to Be Melted, Structure Properties 33

Table 3.2 Example Material to Be Melted, Incident Laser Properties 33

Table 4.1 Computation Time for Various Meshing Methods 50

THIS PAGE INTENTIONALLY LEFT BLANK

CHAPTER 1:
Introduction

Technology is the anvil upon which weapons of war are forged. In the sixteenth century, the age of galleys ushered in large wooden warships armed with rams at their bow, side by side, hurtling into their adversaries. With the adoption of gunpowder on naval vessels, the seventeenth century made warships formidable at range. Gone were the days of slow, heavily fortified bows, with sailors rowing headlong into battle. Instead, swift wooden vessels crowned with vast sails allowed captains to dominate the warships of old with cannon fire. In the nineteenth century, steam-powered warships made of steel outmaneuvered their sail-driven brethren, with their decks of cannons replaced by large-rifled guns able to engage their targets at superior ranges. The age of flight gave way to the crown jewel of naval supremacy: the aircraft carrier. Able to strike targets far past the horizon and able to power-project anywhere in the world, the aircraft carrier became the lynchpin of any naval strategy in the mid-to-late twentieth century. However, all these advances pale compared to what the twenty-first century held for navies across the world.

The increase in computing power and miniaturization of computing technology allowed for smaller and cheaper drones to be manufactured en masse gave way to the use of drone swarms in combat—a slower but more robust strike method able to defeat most kinetic defenses. Additionally, breakthroughs in artificial intelligence and machine learning not only made drone swarms more sophisticated and lethal, but they also allowed missile be designed inherently unstable—and thus, more maneuverable and resistant to kinetic defenses.

From advanced guided missiles to drone swarms, the modern warship is running out of options to defend itself. The prevailing tactic for missile defense has historically been to use a more expensive missile, able to outmaneuver and intercept the attacker at range. What happens when the attacker fires fifty cheap missiles and the defender only has forty-nine interceptors? The result is a sunken warship that costs billions of taxpayer dollars to no avail.

Similar to the previous example, what strategy would the modern warship use against a swarm of drones armed with armor-piercing warheads? A missile per drone, perhaps,

spending millions more per shot to defend than the assailant would use to attack. Once the defending warship has gone Winchester, the attacking ship is free to use a guided missile to sink its adversary. This strategy makes attacking a surface ship cost-effective and defending it unsustainably expensive.

Directed energy (DE) weapons may provide the answer to this seemingly unsolvable conundrum. From high-powered microwaves, to soft-killing sensor dazzlers, to high-energy lasers able to burn a hole through inches of steel, these combat systems are able to weaponize the electromagnetic spectrum at various power levels to defeat various threats. Nearly-endless magazines enable these weapons to attrite large barrages of kinetic weapons, limited only by the power available to them.

These systems have two major weaknesses compared to conventional missiles and other ballistic weapons: their effectiveness is greatly affected by the environment and properties of the target material. Numerous studies over many decades have investigated both of these effects. Propagation studies focus on the environmental effects on DE weapons, such as extinction, turbulence, and thermal blooming, and will be discussed briefly in a later chapter. However, this thesis focuses on damage effects and the ability to simulate them in a three-dimensional environment. By accurately modeling the effects of high energy lasers (HEL) against targets consisting of various materials and complex geometries, engineers are able to better design these combat systems and plan for any warfighting scenario.

1.1 Area of Research

The United States Navy recognizes the importance of simulating warfighting and has established the Modeling, Virtual Environments, and Simulation (MOVES) Institute at the Naval Postgraduate School. This organization has been funded by ONR to model DE engagements at sea and on land and has partnered with various departments across campus to do so. As previously noted and seen in Figure 1.1, propagation and damage effects contribute to a large portion of these simulation efforts.

Atmospheric characterization and HEL beam propagation allow MOVES to properly simulate how a beam is characterized on its target (i.e., irradiance and spot size) which can change drastically from the beam director, as will be discussed in a later chapter. Mission capabilities allow MOVES to properly simulate a ship's ability to engage a target in a

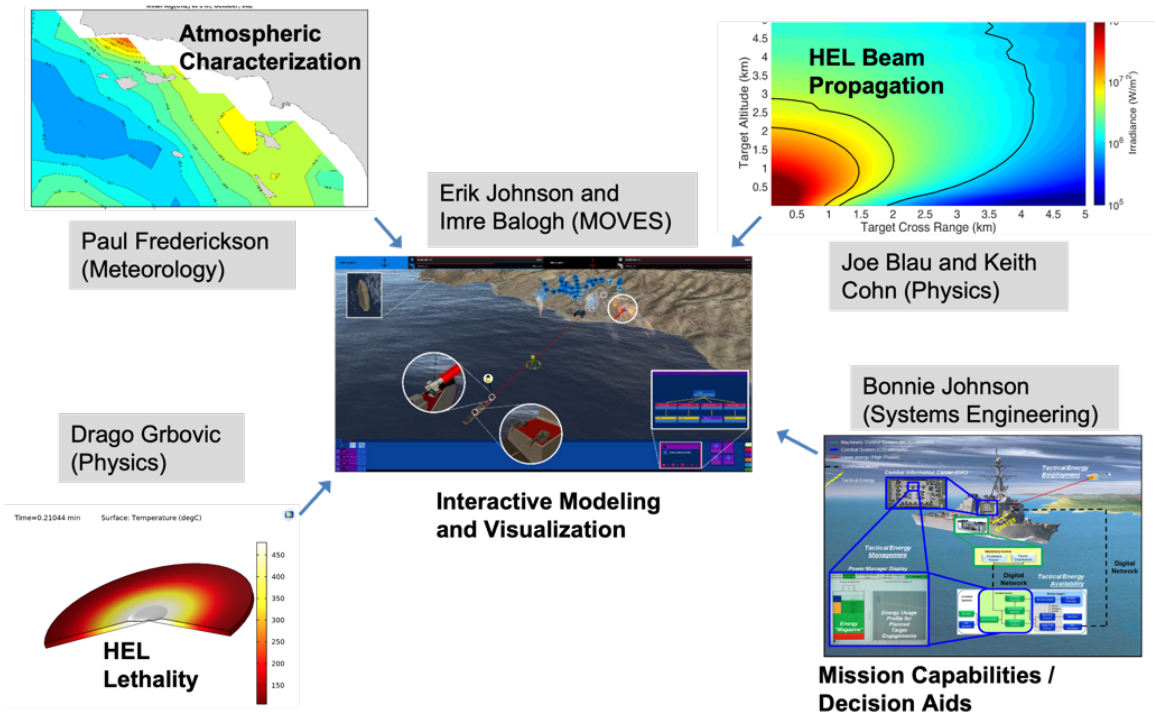

Figure 1.1. NPS Directed Energy Modeling Organizational Chart. Source: [1].

warfighting scenario. Lastly, HEL lethality ultimately determines how much dwell time is required for a high energy laser to defeat its target.

LT Matthew Searight has worked with Dr. Drago Grbovic to great lengths to create a lightweight model that is able to model directed energy engagements that have been verified against experimental data from NSWC Dahlgren. However, this model has been designed to only work with two-dimensional geometries extrapolated to some thickness [1]. By expanding this model to a three-dimensional environment, this thesis will work towards importing externally created computer-aided design (CAD) models and studying them against DE weapons.

Such an effort is monumental, requiring several upgrades from the previous model. In order to complete this thesis in a timely manner, the scope of this study will be limited to the complete development of a three-dimensional model, with a single layer comprised of some material.

1.2 Research Objectives

The two objectives of this thesis encompass the full upgrade of the previous model to three dimensions, ensuring numerical stability and optimizing calculation times of the new model, and to perform a study that was not previously possible in two dimensions. The transition from a two-dimensional model to a three-dimensional model will involve the creation of a movable and orientable beam source, transitioning the damage effects to a three-dimensional Gaussian spread on a curved surface, and studying the effects of choices of meshing methods and error tolerance on validity and calculation times, in a three-dimensional environment. This model will accurately predict laser melting times in this environment and will be validated using experimental data from NSWC Dahlgren as well as the previous two-dimensional model.

Optimization of calculation times, will pinpoint the most optimal modeling methods and how to use them accurately. Several studies performed during the course of this thesis required several days of computation time against a relatively simplistic target. Larger and more complex targets will require exponentially more time, and as such, any reduction in computation time will be essential to timely studies of newly emerging threats. Validation of a simple analytic model could be used to rapidly estimate HEL dwell time for damage of a given target in a real-time HEL engagement model as depicted in Figure 1.1.

Lastly, it was desired to showcase a study in three dimensions, which was impossible with the previous model. Therefore, a study was performed against a curved surface with a non-perpendicular incident beam. These results serve as an example of one portion of a larger engagement scenario and can be used to validate future results.

1.3 Thesis Organization

This thesis will be structured to give a broader sense of Directed Energy, focusing chapter by chapter to the specific task of modeling laser damage effects in a three-dimensional environment. The chapter following this one will provide a brief history of both civilian and military Directed Energy history, giving the reader enough familiarity with the topic to better understand the need for a highly accurate simulation model. This journey through time will review the early stages of laser technology, highlighting the advantages and disadvantages of various laser media as it evolved to where it is today. Followed by a brief

history of the topic, the focus will shift to solid-state laser technology, its current impact on the navy, and plans for the future.

Next, this thesis will briefly discuss atmospheric effects on beam propagation. Although this paper will focus primarily on damage effects, a cursory knowledge of how a beam can be affected at range will be fundamental to the reader's understanding of directed energy engagements in a warfighting scenario. High energy laser damage effects on metal targets will be discussed extensively, as this will be the groundwork for understanding how a model was developed.

With theoretical background knowledge laid, the focus of the thesis will narrow to the specific model that was developed. From this point forward, all studies and discussion will either be unique to the work to develop this model or used to validate it. The studies will start from the ground up, verifying meshing methods and validating from a two-dimensional model, then break away to a study that is only possible using three dimensions.

THIS PAGE INTENTIONALLY LEFT BLANK

CHAPTER 2:
Background

Since time immemorial, warfighters have dreamed of a way to harness light to destroy their adversaries at range. Stories have been promulgated for centuries of Archimedes' mirror weapon [7] burning the sails of enemy warships using sunlight around 200 BCE. These stories have been proven false through historical recreation, demonstrating such a weapon impractical at any useful distance. However, the notion of creating a "death ray" in maritime warfare presented itself as an attractive solution centuries before ships divorced from wind-dependent propulsion.

Nearly 2000 years later, in 1960, Theodore Maiman developed the first spatial and temporally-coherent light amplification device: the ruby laser [8]—a solid state laser plagued by thermal limitations. The laser enraptured the public's imagination, instilled by the science-fiction heat rays dreamed up by H.G. Wells. Immediately, questions of its use as a laser weapon were promulgated through the news media, appealing to the spirit of Archimedes' mirror weapon told over the ages. The genie was out of the bottle, so to speak, and the Advanced Research Projects Agency (ARPA) had its sights set on making a superior laser weapon.

The 1960s introduced the concept of a gas laser, using media such as CO_2 to amplify the optical output. The heat problems shattering the solid-state crystals were mitigated by continuously expelling the gas laser medium, and the output powers achieved were many orders of magnitude larger than any laser could produce before. However, as we will discuss later, the wavelength these lasers could produce were not optimal for atmospheric propagation—causing the range of these weapons to be severely limited. These issues were mitigated with the development of chemical lasers, with a 400kW airborne deuterium-fluoride laser being the first DE weapon to destroy a missile in 1978 [8].

If missile-defeating gas laser technology was developed and tested nearly 40 years ago, why aren't such systems installed on every naval vessel? As we will discuss later, such high-powered lasers are vulnerable to the thermal-blooming phenomena, which causes the power of the laser to spread over a larger area. This effect, combined with the inability to properly account for atmospheric effects and the general unwillingness to store and transport

hazardous chemicals to fuel such lasers, led to the sudden demise of the DE weapon and the lack of a desire to develop it further.

While gas lasers began to wane in popularity, optic fiber technology helped propel research and development once again into solid state lasers. Fast forwarding to the early 21st century, Northrop Grumman revived the use of solid-state Nd:YAG lasers to develop a high-powered DE weapon [5], combining seven slab lasers to output nearly 100kW. This device sported a longer range and abandoned the dependence on highly toxic chemicals that CO_2 gas dynamic lasers required, ultimately reinvigorating government efforts to fund and research DE Weapons. Additionally, advances in commercial fiber lasers allowed the development of DE weapons with better beam quality that were easier to cool than slab solid-state lasers.

2.1 Motivation for Directed Energy

On April 13, 2022, the world watched in awe as Russia's flagship cruiser was sunk off the coast of Ukraine. Although the details are still largely classified, the general details of the attack have been laid out and made public. We currently know that the ship was distracted by Turkish-made, Ukrainian-operated drones, saturating its defensive resources. While vulnerable, the Ukrainian army fired two Neptune missiles set fires that ultimately led to the ship's demise [9].

We can speculate on many details, but the result is clear: drones are now a threat in naval combat. Missile defenses have been outfitted on every modern vessel around the world, but how does one defend against a swarm of drones? Ballistic solutions are not practical against advanced drones, taking advantage of low geometric cross-section and high operational altitudes [10] to effectively evade defense efforts. Missile-based defense is also not feasible, as a large swarm of drones would quickly overwhelm firing solutions and quickly deplete a ship's inventory, leaving it immediately vulnerable to a missile attack. Similarly, a swarm of cheap missiles could be fired at a warship to deplete its inventory, also leaving it vulnerable to an advanced Anti-Ship Cruise Missile (ASCM). The defensive solution to both scenarios requires the use of solid state high-energy laser combat systems.

2.1.1 High-Energy Laser Advantages

Arguably, the biggest advantage of high-energy lasers in a warfighting scenario is their virtually unlimited magazine size. Without requiring constant replenishment like the CO_2 lasers of old, the only consumable required for these weapons is a fuel source—powered from the ship's electric plant. Assuming an extremely conservative estimate of efficiency of 0.3 for both a laser and the gas-turbine generator used to power it, a 600kW laser fired for 5 seconds would require roughly 33 MJ. Since gasoline stores roughly 132 MJ per gallon [11], each shot only requires one-fourth of a gallon. This allows any defending platform to attrite any conceivable swarm of cheap anti-ship cruise missiles or drones as long as the ship's power bus can continuously support the laser's load at a much lower cost than shooting million-dollar missiles at them.

Intercepting missiles require the ability to maneuver at roughly three times the accelerations that an attacking missile could undergo. Because of this, the advanced design and materials required for a defensive missile will always be more expensive than what they are attempting to destroy. In a prolonged conflict, this would ultimately cause more economic turmoil for whoever has more surface vessels to defend. DE weapons do not require any additional configuration or design to engage a highly maneuverable target and, as previously mentioned, are inexpensive to fire.

This point is crucial: a cheap, sustainable way to intercept drone swarms and missiles is required for any conflict against near-peer adversaries. The ability to power project and maintain pressure on an adversary's coastline is dependent on the ability to replenish at sea. A missile-based defense doctrine will require the ability to reload missiles in hostile waters. The U.S. Navy has successfully done so in peacetime [12], but with exotic equipment and not under enemy fire. A strategy could be developed, then, for an adversary to attrite surface forces of their defensive munitions using drone swarms or cheaper missiles, fully aware of their inability to replenish those intercepting missiles.

The ability to replenish fuel at sea is an already well-established evolution that occurs regularly in peacetime using no new or additional equipment. Additionally, the U.S. Navy has over one hundred years of experience refueling at sea [13], including during wartime scenarios against near-peer adversaries. In a modern conflict against such adversaries, logistical capabilities would be stretched thin, and the additional load requiring tenders to

reload missiles at sea could unnecessarily strain surface tenders. Therefore, a major benefit of using DE weapons over kinetic weapons for defensive doctrine is the ability to maintain power at adversarial shorelines without additional strain on logistical networks.

An additional advantage that high-energy lasers possess over their kinetic counterparts is their ability to deliver megajoules of energy to their target at rapid speeds. Although these weapons require a dwell time to inflict significant damage, the initial effects are nearly instantaneous. For comparison, an intercepting missile traveling at an average of Mach 2 would take just over seven seconds to reach a target five kilometers away. High-energy lasers have the capability to achieve a hard kill at the same range in several seconds. Additionally, hitting a fast-moving target requires predicting its location on intercept, which can be a challenging endeavor. The near-instantaneous delivery of energy from a DE weapon negates this point.

Not only are these combat systems much faster to engage their target, but they also are far more precise and accurate than even the most advanced intercepting missile. DE weapons possess bleeding-edge tracking systems that allow them to precisely fire upon vulnerable areas on their target. With the probability of hit very close to 1.0, high-energy lasers provide the accuracy and consistency a defense strategy would require against any swarm engagement.

Lastly, DE weapons possess a force-scaling capability that kinetic weapons cannot replicate. A defensive doctrine can include the ability to scale power down to temporarily blind sensors onboard a target, scale up to permanently blind sensors, or scale up even further to hard-kill a target. This scaling ability allows for much more flexibility in peacetime scenarios without risk of further escalation. Additionally, if a target requires too much time to hard-kill, a soft-kill can be performed on it before moving on to other targets.

2.1.2 High-Energy Laser Limitations

High-energy lasers are susceptible to many countermeasures that would not be of concern to a kinetic weapon. The most simple and effective countermeasure to a DE weapon intending to hard-kill its target is to use a thin, reflective coating around vulnerable points. As we will discuss in more detail later, energy deposited onto a material is dependent on its absorptive properties. Therefore, by using reflective shielding around vulnerable areas, the time to

kill can be drastically increased. For example, if the structural material is 80% reflective, a coating that is 95% reflective would theoretically quadruple the time a higher-energy laser would have to dwell on its target to achieve the same effect. There are caveats to this, but this is a potential weakness of this technology.

Additionally, material choices can preclude the use of DE weapons to hard kill a target in any reasonable amount of time. The use of composites designed to absorb and dissipate a large amount of heat vastly increases the time a high-energy laser would be required to dwell on a target before achieving any lethal effects. Materials such as Pyroceram [14] are often used in nose cones and other leading edges of missiles. Pyroceram is much harder to ablate than other metals, making front-facing shots far more difficult. Crossing shots can also be made more difficult by rolling the missile such that the deposited energy from the laser is spread over a larger area.

The biggest limitation of high-energy lasers, however, is their range. The two main limitations to a DE weapon's range are atmospheric interference and its inherent line-of-sight characteristic. Many factors contribute to atmospheric losses and will be discussed in more detail in a later chapter. However, as a broad summary, DE weapon effectiveness varies drastically with weather and environment. One of the biggest challenges with high-energy lasers remains in how to minimize spot size and enhance irradiance at longer ranges—this will require leaps in development before non-terminal defense will be feasible.

Although a moot point at shorter ranges, as atmospheric effects currently constrain laser range, DE systems are ultimately line-of-sight weapons. Therefore, unlike intercepting missiles, high-energy lasers will never be capable of beyond-the-horizon strikes. Therefore, inorganic tracks to surface vessels will not provide any tactical advantage for using DE weapons vice kinetic solutions against high-speed sea-skimming threats. The combination of line-of-sight dependency and the effects of atmospheric propagation prevent high-energy lasers from making kinetic weapons obsolete. Rather, DE weapons act as an additional layer of defense, to be used primarily against swarm threats and cheaper, less sophisticated missile threats. In a last-ditch effort for defense, however, these weapons can be used along with other terminal interceptors to defeat advanced sea-skimming missiles.

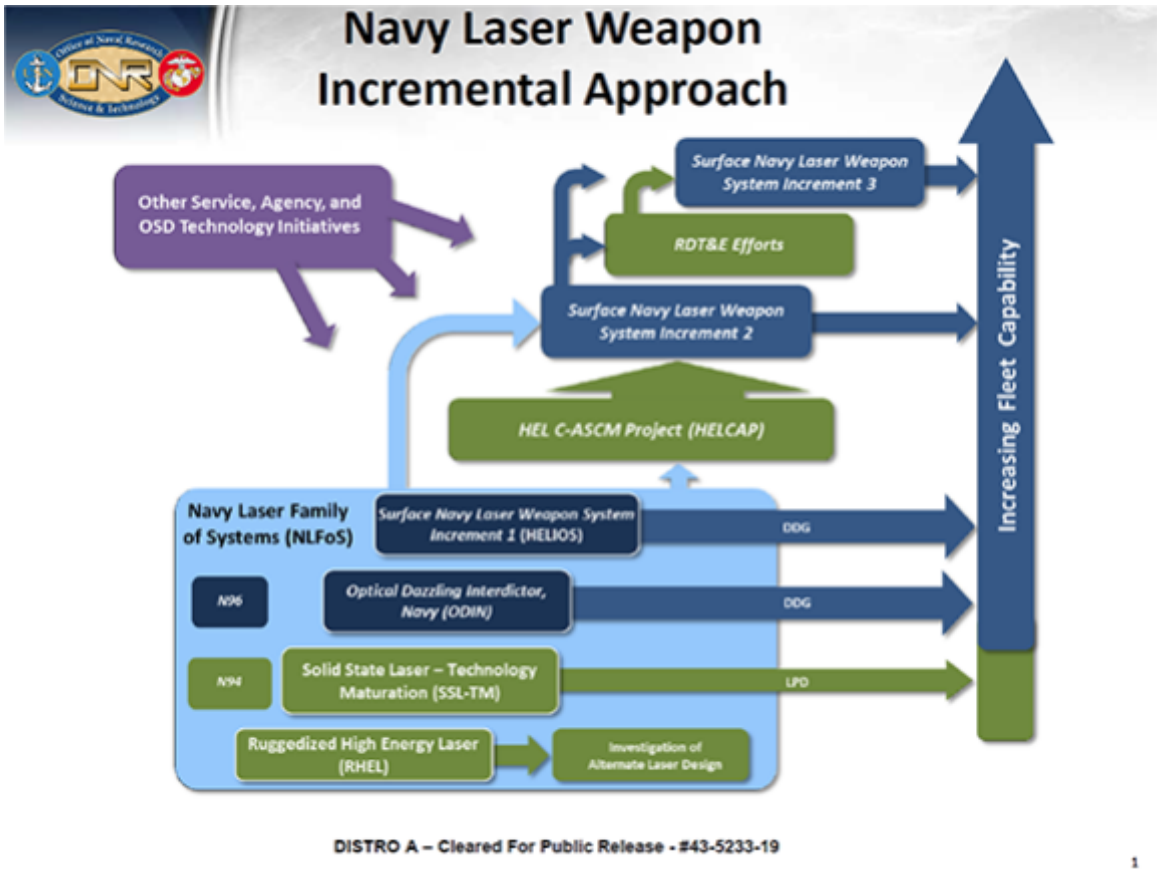

Figure 2.1. Figure B: Office of Naval Research's Incremental Approach to Laser Weapon Development and Installation. Source: [2].

2.2 Navy Directed Energy Programs

Though these limitations provide monumental challenges to any engineer intending to design effective DE weapons, they are not unconquerable. The U.S. Navy has recognized the importance of developing and installing these systems on surface combatants fleet-wide, using a series of milestones to roll out iterative weapons in phases.

Figure 2.1 illustrates the U.S. Navy's approach to increasing the fleet's DE capabilities through phased release. As laser weapons are improved over time, they will be installed incrementally on a select few platforms for operational use at sea. This approach allows weapons to be tested through rigorous environments and encourages a feedback process to rapidly improve future weapons mid-development.

2.2.1 Solid State Laser Technology Maturation

The first DE weapon intended as a prototype for future design was the Laser Weapons System Demonstrator (LWSD), developed under the Solid State Laser Technology Maturation Program. This system was designed and fielded by Northrop Grumman with an output power design specification of 150 kW. It was largely intended to prove capabilities that would be enhanced in later generations, such as counter-intelligence, surveillance, and reconnaissance (C-ISR), counter-fast inshore attack craft (C-FIAC), and counter-unmanned aircraft systems (C-UAS). Figure 2.2 illustrates the location and layout of this system [2], and it was only briefly installed on USS Portland in 2019 for testing. This graphic shows the fundamental components of a laser weapon system, and this layout would be the inspiration for later designs. However, it is worth noting that as a temporary testing apparatus, this system was not integrated into the ship's electrical bus or combat systems. Therefore, standalone power modules were installed below decks, and a control console was installed separately. The beam director can be seen on the ship's bow, raised aloft at some undisclosed height. The advantageous position allows the beam director to have a large angle of operation and minimize optical turbulence from the deck, the importance of which we will discuss later in this chapter.

This system was successful in its development and was able to destroy an Unmanned Aerial Vehicle (UAV) during testing [15]. The Laser Weapons System Demonstrator was removed from the Portland due to successful demonstration.

2.2.2 Optical Dazzler Interdictor, Navy

Naval Surface Warfare Center Dahlgren was tasked with developing a laser weapon system capable of defeating unmanned aerial systems. This system was intended to be a lower-power system with the primary purpose of blinding its adversary's sensors, causing the airborne system to crash or malfunction to the point where it could no longer be considered a threat.

After two and a half years of development, the Optical Dazzler Interdictor, Navy (ODIN) was completed and was slated to be installed on eight *Arleigh Burke*-class destroyers [2]. Staying true to RADM Meyer's mantra of "build a little, test a little, learn a lot," these eight fielded ODIN laser systems will provide valuable feedback for the next iteration for DE

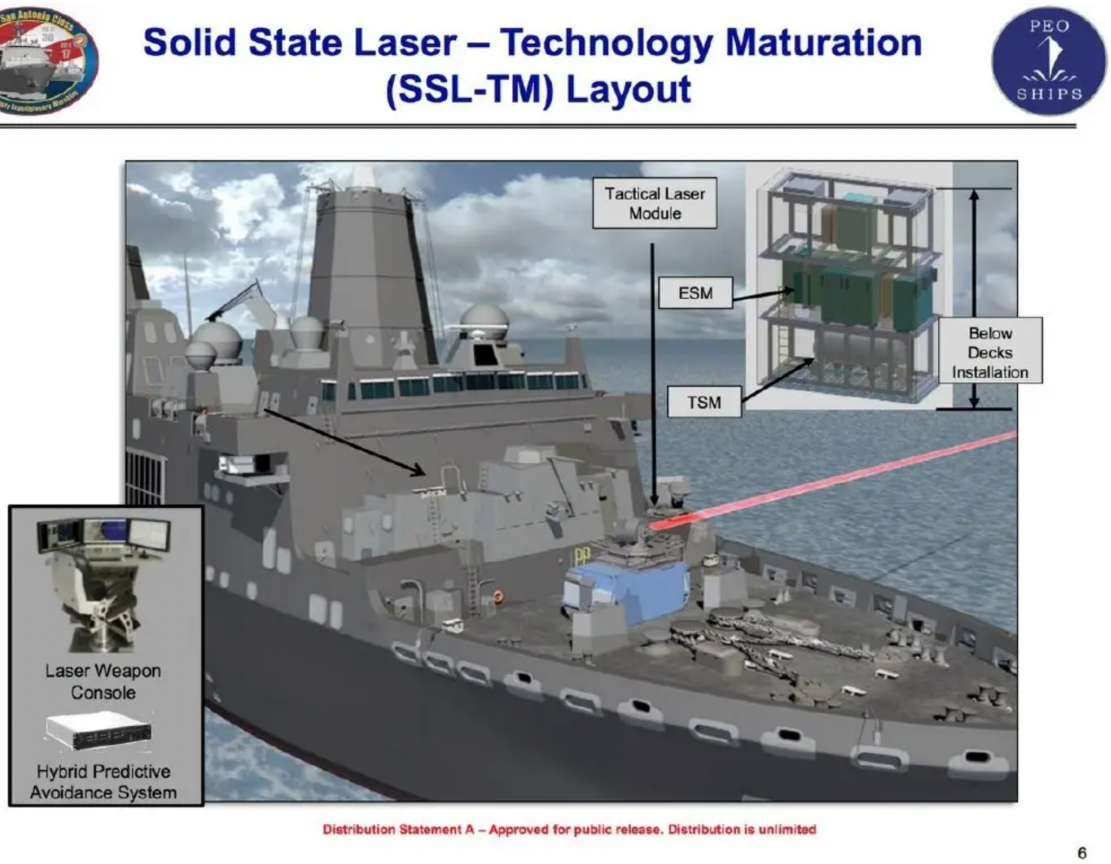

Figure 2.2. SSL-TM Loadout and Configuration. Source: [2].

Weapons: the high-energy laser with integrated optical dazzler and surveillance (HELIOS). The lessons learned from operational use and testing will allow HELIOS to be fielded in a more complete form, precluding testing from retreading the same ground and ultimately delaying a more complete DE weapon from being installed across the fleet.

Figure 2.3 shows ODIN installed on the USS Stockdale just aft of the five-inch gun, allowing for the same advantages the location of the LWSD brought. ODIN installations are intended to be permanent but are not fully integrated into ship's cooling, power, and combat systems. Although not clearly illustrated by this picture, ODIN possesses the same dependency on standalone support systems as the LWSD.

Figure 2.3. ODIN System Installed on USS Stockdale (DDG 106). Source:[2].

2.2.3 Surface Navy Laser Weapon System Increment 1

The Surface Navy Laser Weapon System Increment 1, more often referred to as HELIOS, acts as a natural evolution in the line of DE weapons onboard Navy vessels. By using the engineering and feedback learned from ODIN, HELIOS was able to incorporate dazzling capabilities that complement the high-energy laser installed in this system. The increase of power to 60kW, scalable to 150kW, allows HELIOS to incorporate hard kills into its mission suite by physically burning a hole through its target. Thus, this weapon is able to defeat dazzle-resistant UASs, which are expected to be more expensive, more sophisticated threats.

The ability to choose between soft and hard kills gives HELIOS the flexibility to prioritize dwell times on various threats, giving this system the best probability to defend against a heterogenous UAS swarm. The Navy will begin with installation on Flight IIA *Arleigh Burke*-class destroyers. Still, this system will be unable to be installed on the upcoming Flight III due to the new AN/SPY-6 consuming the extra power that HELIOS would require [2]. Due to this limitation, it is likely that HELIOS will only be fielded through the

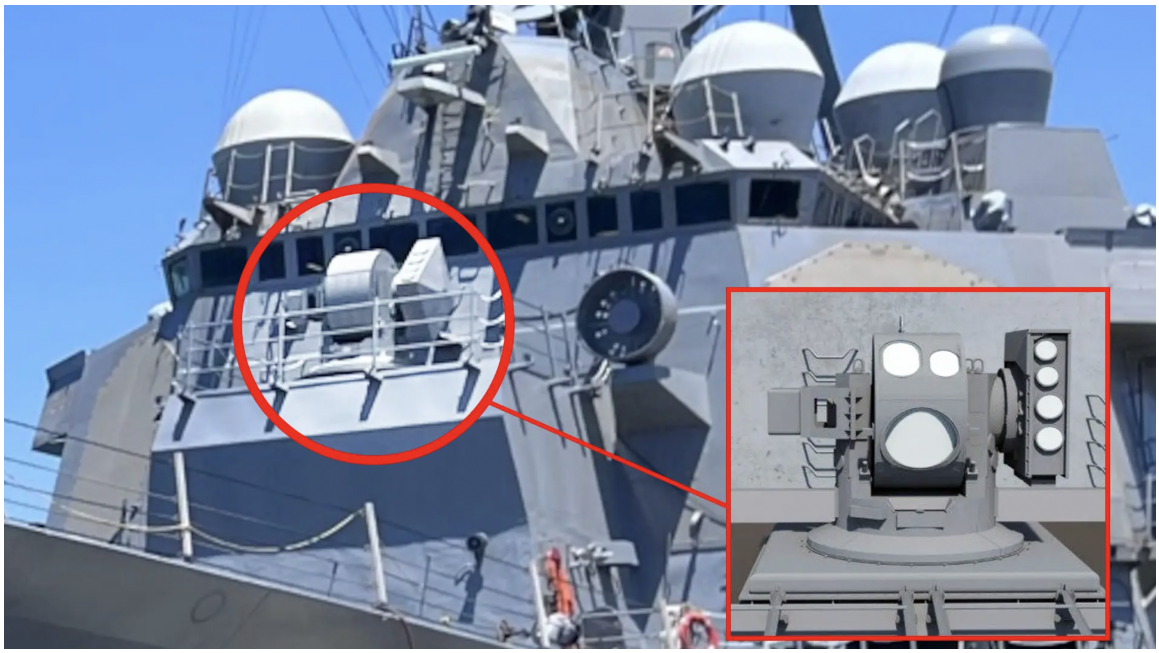

Figure 2.4. HELIOS Location and Beam Director, as Installed on a Flight IIA *Arleigh Burke*-Class Destroyer. Source: [3].

modernization of older ships—currently only being planned to be installed on a single ship, the USS *Preble* (DDG 46). As we will discuss in more detail in the next section, a complete redesign of ship's electric systems must be performed on the next class of destroyers to allow for more powerful DE weapons.

Figure 2.4 shows the different configuration of HELIOS's beam director, which can be compared to ODIN's beam director in Figure 2.3. The newly upgraded beam director illustrates a more complex design, with the optical dazzling portion installed to the side of the high energy laser. The installation of HELIOS has several similarities to its predecessor, with Figure 2.4 showing the location being roughly the same and sporting a very similar supportive platform. However, this system was designed to be far more entrenched into the ship's systems than ODIN or LWSD, fully utilizing ship's cooling and power—even fully integrating into AEGIS, the *Arleigh Burke*'s combat system. Although complicating the system's installation, such platform maturation allows future ship classes to be designed with DE weapons in mind.

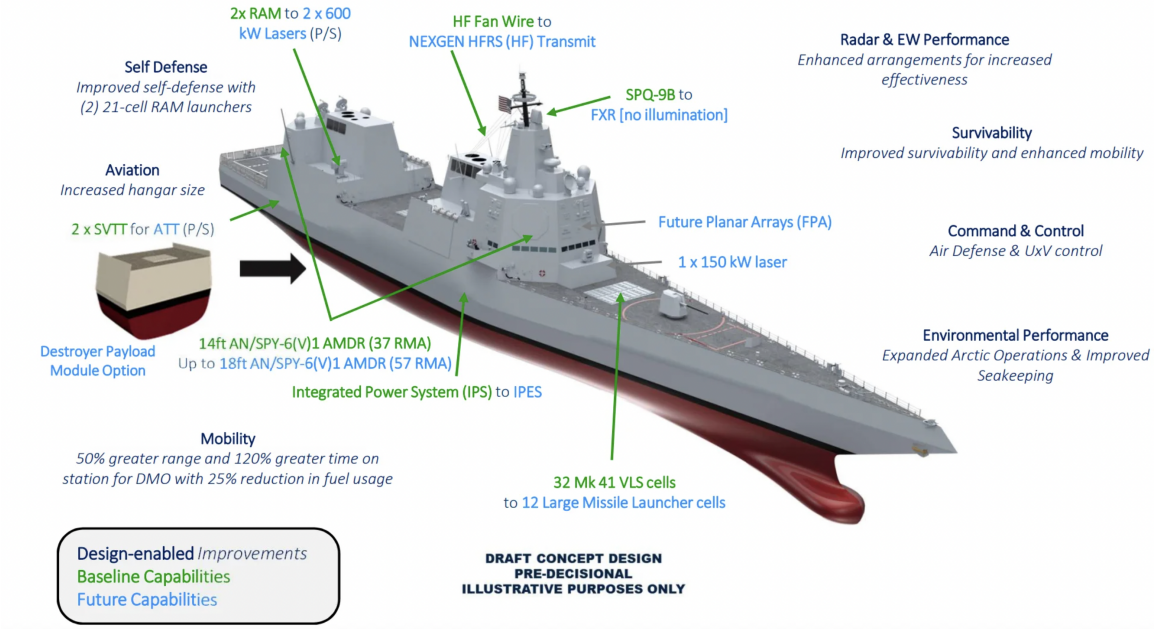

Figure 2.5. DDG-X Concept and Layout. Source: [4].

2.2.4 High Energy Laser Counter-ASCM Project

With the ability to inflict soft and hard kills on UASs, perform C-ISR, and C-FIAC missions, the natural evolution is to gain the ability to target and destroy anti-ship cruise missiles (ASCM). This capability will require more advanced adaptive optics to compensate for atmospheric effects, precise targeting, better beam control, and higher powers of at least 300kW. Although ambitious, these challenges are exactly what the High Energy Laser Counter-ASCM Project (HELCAP) intends to overcome.

Figure 2.5 illustrates the concept and layout of the newly announced DDG-X. As previously mentioned, HELIOS's installation was bottlenecked by the capabilities of the *Arleigh Burke*-class destroyer's electric plant. If 60-120kW DE weapons were not feasible with current designs, a complete redesign would be required for the 300kW+ requirement to defeat anti-ship cruise missiles. As such, the new DDG-X proposes a newly designed integrated power system (IPS) that can handle upgrades for two HELCAP weapon systems to be installed port and starboard aft of the ship's bridge. This new design cements the new laser weapon into ship's integrated defenses, further proving the US Navy's commitment to the development and operatiion of DE weapons.

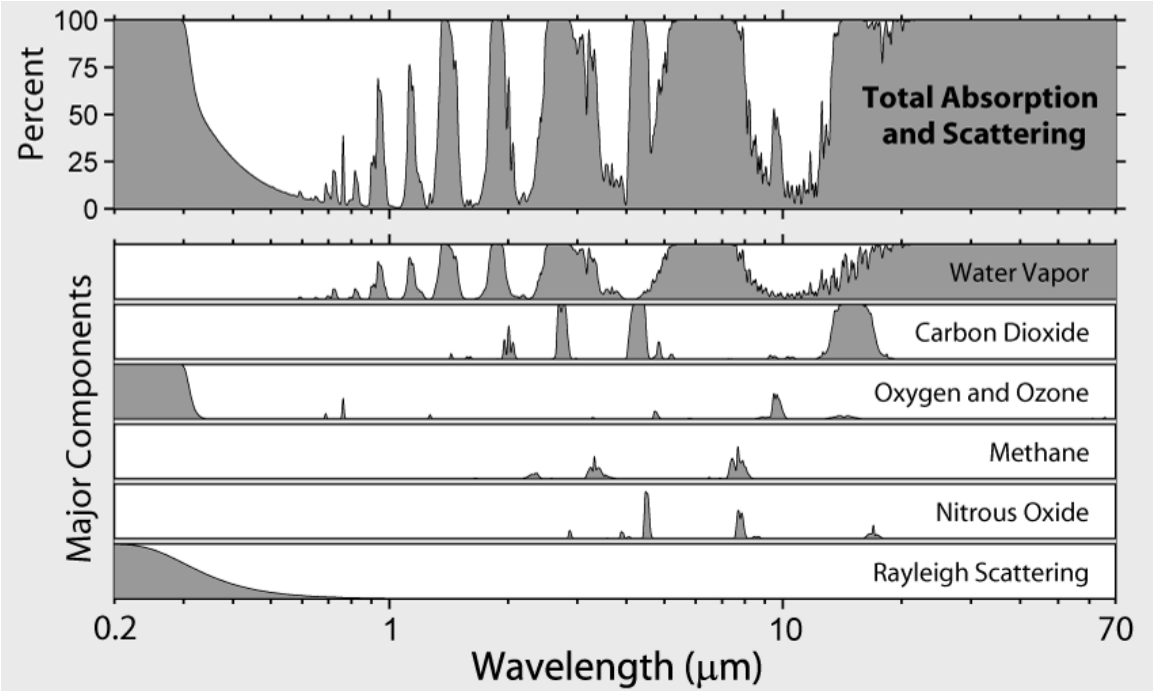

Figure 2.6. Absorption and Scattering Windows as a Function of Wavelength. Source: [5].

2.3 Propagation Effects and Challenges

The biggest factor for a DE weapon's ability to soft kill or hard kill a target is the environmental effects on the beam. Unlike kinetic weapons, photons are subject to scattering and absorption during propagation, causing aerosols and water droplets to greatly affect beam intensity and spot size on target. This section will mostly focus on five factors that ultimately lead to our ability to estimate spot size and irradiance: extinction properties, optical turbulence, thermal blooming, diffraction contributions, and jitter contribution.

2.3.1 Extinction Properties

Photons interact with molecules and aerosols suspended in the air through scattering and absorption. Photons that match the energy level difference between an initial atomic state and some final state have some probability of being scattered or absorbed. Therefore, a collimated beam of photons traveling through the atmosphere can undergo a large amount

of extinction (reduction in power) according to the Beer-Lambert Law,

$$P(Z) \approx P_0 e^{-\int_0^Z \epsilon(z)dz}, \tag{2.1}$$

where $P(Z)$ is the power at some range Z, given an initial power P_0 and an extinction coefficient function of $\epsilon(z)$. This extinction coefficient is a strong function of wavelength; it also depends on the type and concentration of molecules and aerosols along the beam path.

We can see this wavelength relationship to extinction in Figure 2.6, showing near-complete scattering at less than 0.2 microns and complete absorption from water vapor at greater than 20 microns. The areas in between have various "windows" where extinction is at a minimum—this is where a laser beam can effectively propagate. Solid-state lasers are able to emit near 1 micron—where a transmission window exists—while gas-based lasers would all transmit where atmospheric effects were much greater. This again illustrates just how much of an advantage modern solid state lasers have over their predecessors.

2.3.2 Optical Turbulence

In addition to the atmosphere's composition, the heterogenous nature of wind and heat shear can also disrupt laser propagation. Snell's Law, represented by

$$n_1 \sin\theta_1 = n_2 \sin\theta_2 \tag{2.2}$$

describes how as the index of refraction (n) changes for a medium, so will the angle that it refracts a light ray. Therefore, we can observe beams becoming defocused during propagation due to this effect, causing the resulting spot size to be much larger.

By observing the index of refraction at some point $\mathbf{r}$ in the medium, and as it changes over some distance $\mathbf{\Delta r}$, we can characterize turbulence at a point using the refractive structure constant as

$$C_n^2(r) \equiv \frac{\left\langle [n(\mathbf{r}) - n(\mathbf{r}+\mathbf{\Delta r})]^{\,2} \right\rangle}{|\mathbf{\Delta r}|^{2/3}}, \tag{2.3}$$

where $\langle \cdots \rangle$ represents the ensemble average over a sphere of radius $|\mathbf{\Delta r}|$. This parameter can then be used to a characterize turbulence along a laser beam path using Fried parameter r_0

$$r_0 \equiv \left[0.423k^2 \int_0^R C_n^2(r) \left(1 - \frac{r}{R}\right)^{5/3} dr \right]^{-3/5}, \tag{2.4}$$

where k is the wavenumber of the beam, and R is the distance to the target. Although this parameter has other uses, such as determining the range at which a beam has transverse coherence [5], this parameter is primarily used in this modeling to determine the component of beam spot on the target dependent on turbulence, w_t. We can define this turbulent contribution to spot size as

$$w_t \approx \frac{2\lambda R}{\pi r_0}, \tag{2.5}$$

where λ is beam wavelength. All other variables are the same as used in Equation 2.4.

2.3.3 Thermal Blooming

A significant challenge to transmitting megawatts of power through a laser beam is the phenomena of thermal blooming that can cause a high-energy laser beam to defocus as it propagates. This can result in such large spot sizes at long ranges that the intensity can be as low as at it would be at a much lower power. This effect is due to the molecules and aerosols in the air medium absorbing large amounts of photons, causing the air to heat up and change its index of refraction. Since the source of disruption is the beam itself, this produces a positive feedback loop where the longer a beam is propagating along the same path, the more defocused that beam will become. It should be noted that if the beam origin and/or target changes position, the laser beam will interact with new regions of air, which may cause this effect to not be as prominent—making high-energy engagements far more effective. As this phenomenon is difficult to characterize, and this thesis is more focused on damage effects, we will ignore it to simplify our model. However, if this model is implemented into full simulations that include atmospheric effects, it is imperative that this parameter be considered.

2.3.4 Diffraction Contributions

For the purposes of our model, we will assume that the transverse beam profile for all distances from the laser will maintain a near-Gaussian profile with a beam quality factor (M^2) of one. However, a quality factor greater than one should be used in a more realistic scenario, as this is caused by modes inside the laser cavity other than the fundamental transverse mode. Despite engineering efforts, these additional modes can survive inside a laser cavity or optical fiber. These higher-order modes lead to a larger beam quality factor and ultimately, a larger spot size. We can see from the diffraction contribution to spot size,

$$w_d \approx M^2 \frac{2\lambda R}{D}, \tag{2.6}$$

where D is the aperture diameter of the beam director, how a larger beam quality factor (M^2) will result in a larger spot size and therefore lower beam intensity on target.

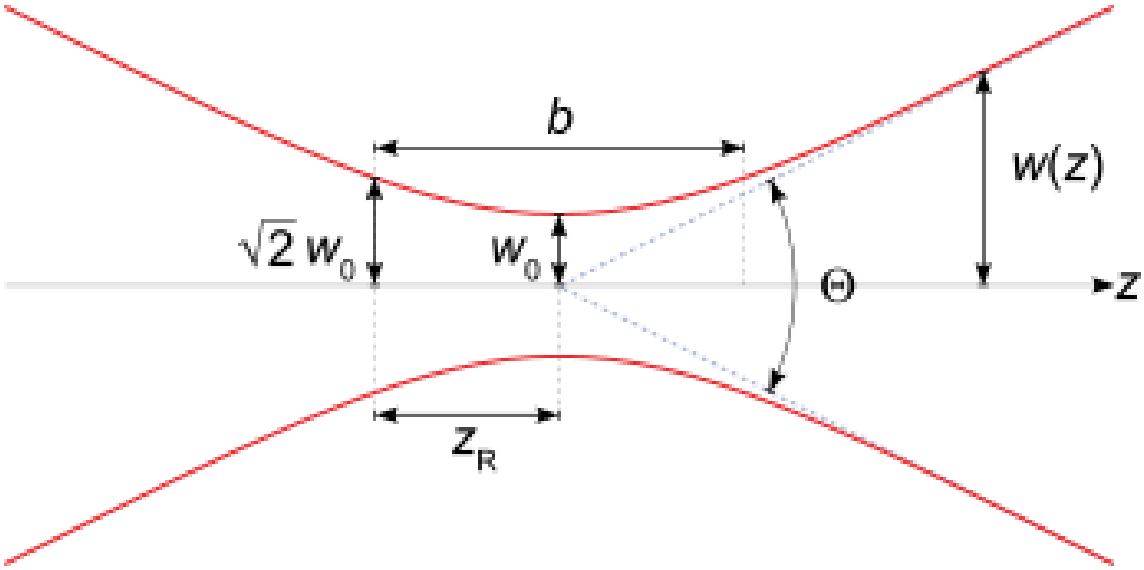

Figure 2.7. Cross-Section of Beam Profile as a Function of Distance. Source:[5].

2.3.5 Jitter Contributions

Especially in maritime environments, the ability to keep a laser focused on a small spot over many kilometers can be affected by sea state and other sources of vibrations on a ship (pumps, motors, etc.). Unfortunately, even the best-stabilized platforms will produce some jitter as a mounted laser fires, causing its beam to wander and spread around its intended target. Through time-averaging of a beam's profile on a target, we can characterize this effect on spot size as

$$w_j = \theta_R R, \tag{2.7}$$

where θ_R is the angular variance due to jitter, which is proportional to the RMS deviation from the intended target over time. This deviation is typically on the order of microradians and can be reduced through advanced gimbal platforms and using proper couplings to reduce vibrational effects on the beam.

2.3.6 Spot Size and Irradiance Estimation

The effects a beam will have on its target largely depend on the amount of irradiance (or intensity) delivered to it, which is defined as the amount of power over a given amount of area. Therefore, a larger amount of power delivered over the smallest possible area will give the most significant damage effects. This parameter will be important for modeling later, and as such we must determine an appropriate way to estimate it. The aforementioned contributors to spot size will be instrumental in this estimation, allowing us to formulate the total spot size on the target through an addition of magnitudes. We can characterize this total spot size (w_Σ) as

$$w_\Sigma = \sqrt{w_t^2 + w_d^2 + w_j^2}, \tag{2.8}$$

where w_t is the spot size due to turbulence, w_d is the spot size due to diffraction, and w_j is the spot size due to jitter. Thus, we can use this equation to estimate the spot size on the target based on atmospheric and laser parameters, as described in the subsections above.

By combining the total spot size determined by equation 2.8 with the power at a distance as solved by equation 2.1, we are able to therefore estimate the irradiance delivered to the target. This time-averaged irradiance, ignoring thermal blooming, can then be estimated as

$$\langle I(Z) \rangle \approx \frac{1}{\pi w_\Sigma^2} P_0 e^{-\int_0^Z \epsilon(z) dz}, \tag{2.9}$$

where $\langle I(Z) \rangle$ is the time-averaged value of irradiance at some distance Z. Equation 2.9 becomes instrumental in environmental modeling, where distances and atmospheric parameters are ever changing.

By assuming the values as outlined in LT Matthew Searight's thesis [1], we can assume a spot size of approximately 5 cm as a typical value for a HEL beam at a range of several kilometers. Additionally, we will assume that the beam output power as being 600kW based on the long-term goals for the HELCAP project. As such, we will look at scenarios where power ranges from 600 to 50kW—realistic power incident on the target depending on atmospheric extinction.

This thesis will not evaluate the effectiveness of high-energy laser weapons on the DDG-X or any other naval platform. Many factors have been simplified for timely completion of the three-dimensional model associated with this thesis, to include the omission of tactics, techniques, and procedures, as well as the omission of any data associated with foreign threats such weapons may be used against.

CHAPTER 3:
Damage Effects of Directed Energy

3.1 Targeting

In order for any weapon to maximize its effectiveness, it must be able to ensure a hit, optimize the chance of damage given a hit, and optimize the chance of kill given damage. For kinetic weapons, these parameters will play a vital role in targeting system design and warhead design to ensure lethality. For DE weapons, we can assume the hit is nearly guaranteed once a track has been established—however, the location of beam placement is vital to optimize damage.

With the precise nature of DE weapons coupled with modern targeting systems, the ability to analyze a laser weapon's effect on specific targets is imperative. In order to minimize the classification of this thesis, specific targets will not be used. Instead, generic targets will act as characteristic examples of UAS and ASCM threats.

Unmanned Aircraft Systems pose one of the biggest threats to naval vessels in the 21st century. However, their inability to execute high speed maneuvers and their reliance on sensors makes them vulnerable to DE weapons. First, let us examine a non-military drone that might be developed to conduct ISR missions for attack drones.

Figure 3.1 shows a DJI Phantom Pro V2, which has been seen in the 2022 Ukraine conflict as conducting ISR missions and has also been modified to release grenades from an elevated height. These inexpensive non-military systems can pose a large threat, as they can be bought and sold with little to no oversight and can be used en masse to ensure reliability. As such, a DE weapon proves an ideal candidate to defeat such threats.

As an ISR UAS, the most vulnerable portions of the system will always be its onboard sensors. A DE weapon with low power can blind onboard sensors, either temporarily or permanently, providing a soft kill for this threat. However, if we were to assume that this system has been weaponized with some warhead, we might also assume that the threat has been improved with home-on-jam capabilities. This capability would allow the UAS

Figure 3.1. DJI Phantom Pro V2. Source: [6].

to continue toward the location of the DE weapon and detonate its warhead, potentially disabling it so that other threats can advance unfettered.

In this case, a hard kill will be required to eliminate this threat. If a DE weapon were to increase its output power, structural damage could be imposed on the UAS. However, in a swarm scenario, dwell time would need to be minimized on each threat to ensure that an attack would be unsuccessful. Each UAS will therefore need to have a developed threat vulnerability model that integrates with onboard targeting software. This will allow the DE weapon to quickly melt or vaporize components of the threat so that it can no longer advance toward its destination before moving onto the next threat. In the case of a quadcopter, the propellers are balanced such that all four rotors must operate in tandem to maintain flight. Therefore, damaging a single rotor on this system will render the whole quadcopter inoperable and force it to land.

In addition to UASs, ASCMs and ASCM swarms pose a significant threat to surface ships and shore-based defenses. With rocket motors onboard, the reaction time required to

defeat these threats is much shorter and therefore requires similar vulnerability models as mentioned previously. ASCMs with onboard sensors have the same vulnerability as UASs with regards to soft kills, but they also have the capabilities to home-on-jam. However, as they are flying at supersonic speeds and engineered to fly with strict tolerances, ASCMs are vulnerable to changes in missile dimension and heat profile. This vulnerability once again makes DE weapons a potential solution to such a threat.

DE weapons have the ability to melt through the skin of such missiles, pinpointing critical targeting systems, or even prematurely detonating the warhead. Inducing these stresses on an already stressed missile fuselage can also cause warping and deformation that can lead to instabilities in the system such that it will no longer be able to stay in flight. This phenomenon means that total melting of the system is not necessarily required to defeat such a threat. For the purposes of this thesis, however, we will consider how a 5 mm thick metal surface would deform without regard to structural, thermal, or aerodynamically induced stresses. This metal is not representative of any particular alloy, but the model can simulate any metal on a realistic target such as aluminum, steel, titanium, or magnesium.

3.2 Laser-Induced Heating and Heat Transfer in Metals

The ultimate mechanism by which laser weapons damage their targets is by thermal damage. Though this damage is not always caused by melting, as mentioned by thermal induce stresses above, this thesis will primarily focus on melting and ablation effects. Before we consider a target at temperatures greater than its melting point, we must first examine the methods by which this will occur.

First, we will examine the initial radiative heat transfer between the laser and the target. Photons are absorbed into the surface of the target, penetrating to some optical absorption depth [16]. The photons that interact with electrons in this region are absorbed or reflected depending on the absorptivity (A), a value that predicts the absorbed power fraction relative to incident power. The photons that are not absorbed are those that undergo a scattering event, or are absorbed and immediately reradiated at an angle that can no longer interact with the metal target. In either case, these photons are removed from the system in a way such that they are may be ignored.

The photons that are absorbed ultimately cause material temperature to rise in a location

which we will treat as the source of heat in the material, which will extend to the optical absorption length in the case of D-band metals [16]. In the case of S and P-band metals, this region will extend to the ballistic range—the range at which motion of excited electrons may no longer be considered, also characterized as the mean free path of electrons in that material. In either case, we will characterize the region at which electron collisions occur as a result as photon interactions as having some skin depth. This region will act as the source for all heat diffusion equations to the bulk of the structure moving forward.

In order to investigate the power deposited onto a structure over time, we can use the equation

$$P_{\text{net}} = P_{\text{abs}} - P_{\text{loss}}, \tag{3.1}$$

where P_{abs} is the incident power multiplied by absorptivity and P_{loss} is the total sum of energy lost due to radiation, conduction, and convection. The first contribution to P_{loss} that we will explore is the heat loss due to conduction as described above. This rate of change of energy in this region may be estimated as

$$P_{\text{cond}} = k a_{\text{cond}} \frac{T_{melt} - T_{amb}}{\Delta r}, \tag{3.2}$$

where T_{melt} is the melting temperature of the structure, T_{amb} the ambient temperature, a_{cond} is the surface area over which conduction occurs, and Δr is the distance of the temperature gradient. For this case, we will consider a_{cond} to be defined as the area where the edge of the beam intersects with the structure.

In the case of the initial heating of the surface, we observed a phenomenon where electrons are excited or freed from a bound state through the photoelectric effect. Freed electrons would then undergo collisions to excite electrons further in the material, causing them to achieve the same result but through diminishing magnitudes as this event repeated. There is a probability when such electrons de-excite that they will not produce lattice vibrations, characterized as phonons, and will instead emit a photon. These photons can be reabsorbed in the bulk of the structure, causing no net loss to this system. However, they can also be

emitted from the surface of the area of interest to surrounding systems such as to ambient. In our case, we will only consider the surface adjacent to ambient as the radiative loss surface.

We can treat the surface where the beam irradiates the structure as some disc with beam width w_Σ and some skin depth δ. As this region is the only point where direct photon-electron interactions occur, we will also consider it the only volume which radiates directly to the environment. If we ignore conduction for the moment, we can characterize the energy change density in the target [17] solely due to radiation as

$$\rho c \delta = -\varepsilon\sigma \left(T^4 - \frac{A}{\varepsilon} T_{amb}^4 \right), \tag{3.3}$$

where ε is the emissivity of the material, c is the speed of light in the medium, and σ is the Stefan-Boltzmann constant $5.670374419 \times 10^{-8} Wm^{-2}K^{-4}$. By integrating over the surface of the structure, we can determine the energy loss for the system as

$$P_{rad} = \varepsilon\sigma a_{surf}(T^4 - \frac{A}{\varepsilon} T_{amb}^4), \tag{3.4}$$

where a_{surf} is the surface area of the region of interest. Note that in thermal equilibrium, A and ε are equal values, but we will maintain it in the equation for now to present a generalized solution. This formulation allows us to estimate the losses due to photon emissions from the system to the environment and will be of interest in materials where emissivity is large.

Convective loss is the heat loss mechanism associated with fluid flow or loss to the environment due to density mismatch. As air is not characterized for any portion of this thesis, including atmospheric losses to beam power, we will not consider this loss in any regard. Further work must consider this loss mechanism to create more realistic models.

We will consider the types of losses discussed above to be uncoupled due to weak coupling interactions [17], allowing us to determine the loss mechanisms separately and then add them together, resulting in the total heat loss of the system. We can then characterize each element's power gain as originating from direct radiation of the beam or conduction from another element. Each element's power loss will be due to the two loss mechanisms as

conduction to another element or by radiation to the environment. We will not consider internal radiative transfer within the bulk of the structure due to the symmetry of this mechanism between elements. To further simplify this model, we will only consider losses due to conduction—assuming these losses to be far more significant than radiation in the material we examined. This is due to the high conductivity and low emissivity of the material we examined. Other materials that have low conductivity and high emissivity will need to have radiation losses incorporated into the model simulating engagements with them.

With conduction being the only heat loss mechanism each element is subjected to, we can easily determine the temperature of each element at any given point in time through the equation

$$\frac{\delta T}{\delta t} = \frac{k}{\rho C_p}\nabla^2 T + \frac{S}{\rho C_p}, \tag{3.5}$$

where C_p is the specific heat capacity of the structure under constant pressure, causing the last term to ultimately represent the source's contribution to temperature change in the material. This three-dimensional equation lets the elements in a structure interact with each other through conduction, where the gradient of heat will transfer from the irradiated source volume at the surface, with width w_Σ and skin depth δ, to the bulk of the structure. This will allow us to evaluate the temperature profile over the entire structure as a function of time, which will be relevant in the next section, where we will begin to discuss melting. This will be the sole mechanism we will consider for structural failure.

3.3 Damage by Melting

Now that a method to determine temperature gradient has been established, we can begin to discuss melting. The first law of thermodynamics states that

$$Q_{abs} = \Delta U - W, \tag{3.6}$$

where ΔU is the change in internal energy, Q_{abs} is the total heat absorbed, and W is the

work performed on the system—typically by expansion of the system. Since metals do not expand appreciably as a function of temperature [18], we can therefore approximate that any energy absorbed outside of phase transition will be deposited into the internal energy of the structure—this can be described as a change in temperature, as represented by

$$Q_{abs} = mC\Delta T, \tag{3.7}$$

where m is the mass of the element being considered and C is the specific heat capacity of the material. This equation predicts a linear rise in temperature of some element of a structure, neglecting all losses in the system. This holds true until the solid structure reaches its melt temperature, which represents the maximum amount of excitation the structure can hold before phase transition starts to occur.

Once the element in consideration has reached its melt temperature, the energy imparted to that element will begin to break the intermolecular bonds of the structure's lattice, rather than simply exciting bound and freed electrons. The ordered lattice of the metallic structure will then become broken, and molecules will be free to move in all directions. We can describe this phenomenon as a solid-to-liquid phase transition and can no longer neglect the work term in equation 3.6. All energy absorbed by the structure during phase transition will be used to expand the structure [18], causing no change in internal energy and thus no change in temperature. Therefore, the temperature of the structure will remain constant during phase transition. As we will assume the melted material will be removed promptly after phase transition—and is therefore ablated—the highest temperature we will see during energy deposition will be the melting temperature.

Assuming the element of concern is at melting temperature, we can represent the additional energy required to melt (Q_{melt}) the mass of an element of the structure (m) as

$$Q_{melt} = Hm, \tag{3.8}$$

where H is the latent heat of fusion. This parameter ultimately describes the energy required to expand the element from a solid to a liquid, as discussed above. By combining equations

3.6 and 3.7, we can determine the total amount of energy (Q_{tot}) to raise the structure to melt temperature, and subsequently ablate it. This can be determined by

$$Q_{tot} = m(H + C\Delta T) - Q_{loss}, \tag{3.9}$$

where Q_{loss} is described as the total amount of energy lost over a period of time, as described by the loss mechanisms in the previous section. Our model will consider loss by conduction to outside the region of interest; however, if we ignore this term momentarily, we can approximate the time to melt this portion of our structure.

By lasing the structure with some absorbed power P_{in} , described as

$$P_{in} = \frac{Q_{in}}{t} = IAa \tag{3.10}$$

where Q_{in} is the energy deposited over some given time t, we can begin to approximate time to melt, and I is the irrandiance of the beam. By setting Q_{in} equal to Q_{abs}, assuming no loss to outside regions of the structure, the time to reach melting temperature (t_m) can therefore be described as

$$t_m = \frac{\rho dC}{IA}(T_{melt} - T_0) \tag{3.11}$$

where the portion to melt has cross sectional area $a$and depth d and mass $m = \rho ad$, given an initial temperature T_0. The time to reach melting (t_M) can therefore be described as

$$t_M = \frac{\rho d}{IA}(H + CT_{melt} - CT_0) \tag{3.12}$$

which will represent a fair approximation to compare values to during modeling.

Let us consider some structure and incident laser with the following characteristics:

By setting spot size (w_Σ) equal to the radius of the structure (a), plugging values from tables 3.1 and 3.2 into equation 3.12, will allow us to estimate the time to melt this structure as

Table 3.1. Example Material to Be Melted, Structure Properties

Density (ρ)	$2700\frac{kg}{m^3}$
Thickness (f)	$5mm$
Absorptance (A)	0.2
Heat Capacity (C)	$960\frac{J}{kgK}$
Latent Heat of Fusion (H)	$40000\frac{J}{kg}$
Initial Temperature (T_0)	$273K$
Melting Temperature (T_{melt})	$750K$

Table 3.2. Example Material to Be Melted, Incident Laser Properties

Irradiance (I)	$2 * 10^7 \frac{W}{m^2}$
Total Spot Size (w_Σ)	$5cm$

approximately 3.4 seconds. This value will act as a valuable benchmark with which to compare our model.

THIS PAGE INTENTIONALLY LEFT BLANK

CHAPTER 4:
Model Setup and Methodology

HEL lethality models typically examine one aspect of physics, specifically focusing on ablation, heating, etc. The eventual goal of this research is a more complete model that accounts for fluid mechanics of air, structural stress, ablation, and flight dynamics. As such, modeling software involving the use of multiphysics is required. COMSOL is a powerful simulation environment designed to help researchers and engineers simulate real-world effects. By including multiple physics models, such as thermodynamics, mechanics, and fluid dynamics, COMSOL lets us easily replicate such a complex physical system. COMSOL also can import CAD models of a target, allowing us to model directed energy engagements against specific threats.

4.1 Assumptions and Scope

As discussed in the previous chapter, many simplifications were made to complete this thesis in a timely manner. Future work will be performed to advance this model to incorporate physics that will ultimately allow an end user to accurately predict and optimize the time to kill a threat. The original version of this model was developed by LT Matthew Searight in conjunction with Naval Postgraduate School faculty. It was limited to a simplified engagement of a laser beam on a symmetric flat plate. The goal of this research is the evolution of the previous model from a two-dimensional model to a three-dimensional model fully capable of importing a CAD file and evaluating the time to melt through that target with an incident laser beam. We will start with similar assumptions that LT Searight used [1]:

- Only conductive heat losses will be considered. As such, this model will only be accurate for materials with high thermal conductivity and low emissivity.
- The material is bare, unpainted, polished, and not affected by any layers deeper than the region of interest.
- All material parameters are temperature independent. This is a gross exaggeration, but due to the complexity of this subject, this is likely the topic of an entire thesis. LCDR

Brian Curran, NPS is currently researching these effects and seeks to incorporate them into this model.

- The melted material is ablated and does not affect future heat calculations.
- Other physical effects such as aerodynamic and thermally induced stresses are not yet implemented. Therefore, material ablation is strictly due to the effects of a laser beam incident on its surface.
- The incident laser beam will have an ideal Gaussian profile.

4.2 Governing Equations

For this model, we will consider the deposited beam power to be

$$P_0 = I_0 A \pi r_0^2, \tag{4.1}$$

where I_0 is the incident peak irradiance, A is the absorptivity of the material, and r_0 is the incident beam's spot size, defined as $\frac{1}{e^2}$. This beam power can be introduced to the material via a function in COMSOL called "Deposited Beam Power," which allows us to set the origin and orientation of a beam—a necessity for modeling in three-dimensional space. This function is ultimately represented as a three-dimensional Gaussian profile

$$f(\vec{O}, \vec{e}) = \frac{1}{2\pi\sigma^2} e^{-\frac{d^2}{2\sigma^2}}, \tag{4.2}$$

where $\vec{O}$ is the vector defining our beam origin point and $\vec{e}$ is the vector defining our beam orientation. Therefore, we can determine the profile for the position on a surface ($\vec{x}$) as a function of some relative position (d) in the gaussian heat profile as defined by

$$d = \frac{||\vec{e} \times (\vec{x} - \vec{O})||}{||\vec{e}||}. \tag{4.3}$$

The standard deviation of the beam profile (σ) is related to the beam radius by

$$\sigma = \frac{r_0}{\sqrt{2}}. \tag{4.4}$$

Ultimately, this allows us to determine the heat deposited on the surface of our structure at any given point as

$$-\vec{n} \cdot \vec{q} = P_0 f(\vec{O}, \vec{e}) \frac{|\vec{e} \cdot \vec{n}|}{||\vec{e}||}, \tag{4.5}$$

where $\vec{n}$ is the normal vector to the surface, and $\vec{q}$ is the conductive heat flux vector, characterized by Fourier's law,

$$\vec{q} = -k \nabla T, \tag{4.6}$$

where k is the thermal conductivity of the material. The boundaries of the structure will not lose heat in any direction since we assume thermally insulated boundaries. By setting Equation 4.5 to zero at the boundaries (thus creating an insulating boundary condition), we can ensure that deposited beam power will flow within our structure and will not escape through re-radiation or convective losses to the environment. Additionally, we must ensure that the lased target is large enough to avoid thermal constraints by the edges, as they are not modeled at this time. Empircally, we found that a target radius greater than 3 times the beam radius was sufficient to prevent such edge effects.

Subsequently, the thermodynamic equations discussed in the previous section are implemented to model heat conduction. Equation 3.5 will ultimately govern heat flow through the target but is characterized in COMSOL as

$$\rho C_p \frac{\delta T}{\delta t} + \nabla \cdot \vec{q} = S, \tag{4.7}$$

where S is the heat source per unit volume.

Melting is not a function that COMSOL directly supports. Therefore, we will introduce a fictitious heat flux that we call the "ablative heat flux," and a prescribed mesh velocity will

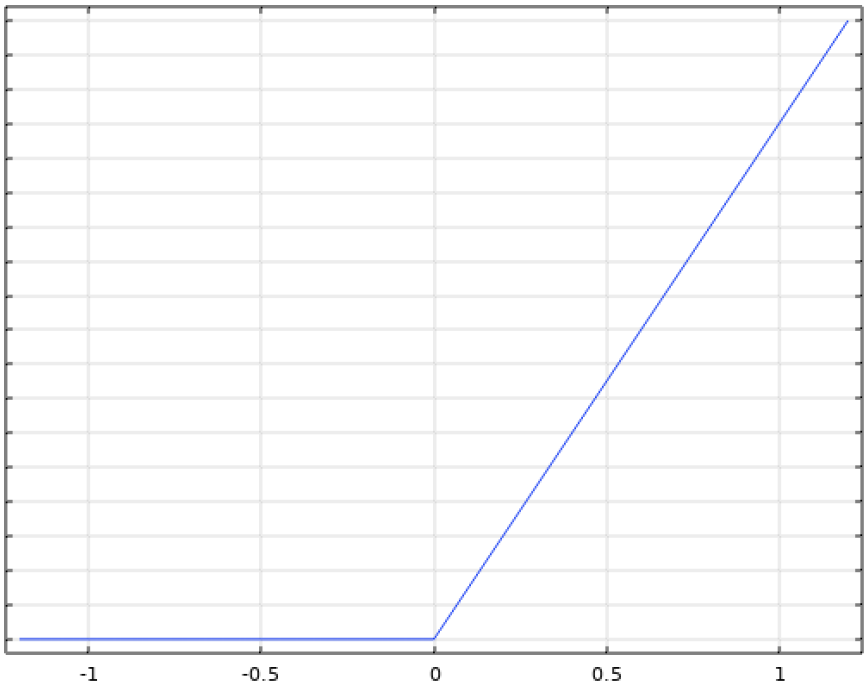

Figure 4.1. Heat Transfer Coefficient vs. Temperature for $\Gamma = 3 * 10^5$

allow us to accurately predict melting in our structure. The energy that would bring the temperature of the structure above the melting temperature (which COMSOL would allow) needs to be removed from the system "manually"—this is will be captured using an ablative heat flux, which satisfies

$$-\vec{n} \cdot \vec{q}_{\text{ablate}} = h(T_{\text{melt}} - T), \tag{4.8}$$

where h is the heat transfer coefficient, given by

$$h(T) = \begin{cases} \Gamma T & T \geq T_{\text{melt}} \\ 0 & T < T_{\text{melt}} \end{cases}, \tag{4.9}$$

where Γ is defined as the ramped coefficient as illustrated by Figure 4.1. Γ is the slope of the curve for $T \geq T_{melt}$.

Since melting is not a supported function in COMSOL, temperature cannot be fixed to some value to simulate energy input being transferred to the expansion of the material rather than increasing internal energy. This function will observe the temperature of an element of the structure and transfer energy out of the material based on the deviation from melt temperature. While the temperature is below melting temperature, this function and the related energy outflow will be zero. As we will see in a later subsection, the slope of this function will greatly affect deformation accuracy and whose optimal value is determined through a series of numerical studies.

Once the temperature reaches the structure's melting point, we can also start to model the deformation of the structure. Now that we have accounted for the energy subtracted from the structure from the phase change, we assume the amount of material that transitioned to a liquid as removed from the system. However, COMSOL does not support deleting portions of a mesh—instead, we must characterize the loss of this material as a moving or deformed mesh. Therefore, we will simulate the ablation of the material by transforming the leading of edge of the mesh lased by the incident beam with a characteristic melt velocity. By allowing the area of interest to be freely deformed, we can characterize the deformation of this mesh by setting the velocity of the mesh in the $\vec{e}$ direction ($v(\vec{e})$,T) as

$$v(\vec{e},T) = \begin{cases} -\frac{1}{\rho H}(\vec{q}_{\text{ablate}} \cdot \vec{e}) & T \geq T_{\text{melt}} \\ 0 & T < T_{\text{melt}} \end{cases}, \tag{4.10}$$

where $\vec{q}_{\text{ablate}}$ is the heat flux vector out of the material that would raise the material past melting point if not removed, and H is the latent heat of fusion. This value allows the mesh to move realistically as the material melts. As we will discuss in a later subsection, however, this can cause mesh singularity errors if the surface of the mesh collides with any other boundary. We will account for this by melting only up to some small distance away from the back boundary before terminating the simulation. As we will see later, this is acceptable due to the linear fit for mesh velocity shortly after the initiation of melting.

4.3 Evolution from Flat Plate

The geometries considered prior to this thesis were restricted to an axially symmetric flat plate with only radius and thickness being adjustable geometrical parameters. This geometry is not ideal for simulating realistic scenarios such as a cylindrical missile frame. Therefore, an evolution from a flat plate to three dimensions was required. COMSOL's robust modeling module exhibits the same fidelity as industry-leading CAD software. COMSOL also allows the user to import CAD files, such as a particular missile.

The logical first step in transitioning to a three-dimensional plate was to model the same disc as the previous model in a 3-dimensional environment and ensure the melt times matched. By modeling the flat plate as seen in Figure 4.2 with the same attributes as listed in tables 3.1 and 3.2, we produced a time to melt consistent with the 2-dimensional flat plate model: approximately 2.9 seconds. This result was achieved by tracking maximum mesh displacement from the surface until it reached 80% of the plate thickness and then using a best-fit approximation to extrapolate to 100% mesh displacement to simulate full melt-through. This method is required to avoid mesh singularity, which is a phenomenon that occurs when two mesh elements occupy the same space, causing errors in calculation that will ultimately cause the simulation to crash. It is also worth noting that both results are supported by the first-principles approach, which estimated a melt-through time of 3.4 seconds. The discrepancies in these two results are due to the assumptions made in the first-principles approach as made in the previous chapter.

Once our model was validated in this way, the next step was to begin transitioning to a cylindrical geometry. This would ultimately allow us to characterize a beam on a missile fuselage and begin to test the accuracy of how a beam might act on a CAD-imported model. The first step in this transition was to curve our disc, as seen in Figure 4.3, and vary the radius of curvature to verify the melt times were nearly the same for those geometries.

As we can see in Figure 4.4, the results for simulated radii of curvature match the results for a flat plate: the time to melt increases linearly with thickness, which also agreed with analytic model predictions. The only stipulation we see is that the radii of curvature begin to affect melt times at larger thicknesses, which could be a physical result but may also indicate numerical error. As this phenomenon could not be directly explained, transitioning from the curved plate to a full cylinder where edge effects were negligible was necessary.

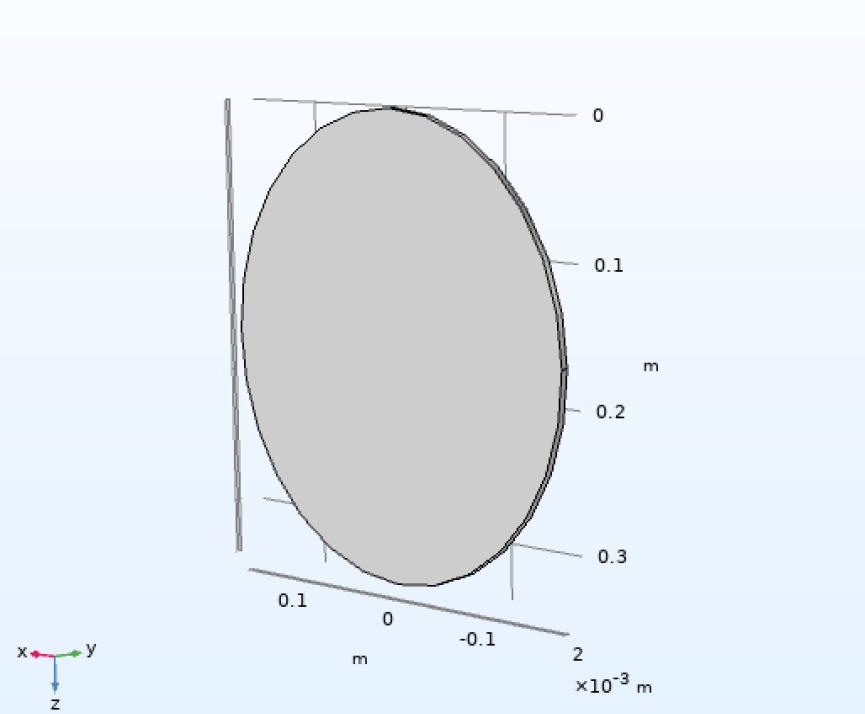

Figure 4.2. Three-Dimensional Flat Plate in COMSOL

Transitioning to a full cylinder made the numerical error suspected in Figure 4.4 obvious. The dashed lines in Figure 4.5 represent the curved plates, whereas the solid lines represent full cylinders. All geometries represented in this figure have a radius of curvature of 300mm, their thicknesses ranging from 1 mm to 5 mm, as described by the legend. The y-axis represents the percent of mesh displacement, where 100% represents a fully-melted through target. As we can see in Figure 4.5, as geometries became larger and more complex, the numerical error induced in the system became far more apparent.

The shape of the displacement over time curve is more accurately represented by the dashed lines, which describe the melt of a curved plate. Equation 3.5 illustrates a flow of heat away from the highest temperature point on the surface, which would cause a less-than-linear melt speed. As melting begins, the material is still largely in a transient state where much of the heat has not reached all the portions of the material within the region of interest. Additionally, we would expect the transient times with less-than-linear melt velocities to be longer for structures of larger thicknesses. As melting continues, the material will transition

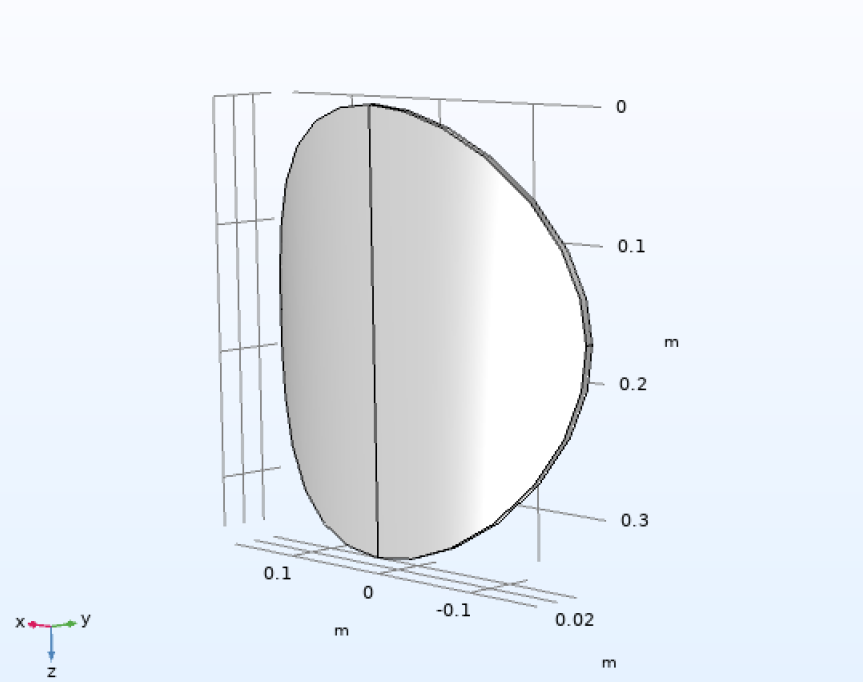

Figure 4.3. Three-Dimensional Curved Plate in COMSOL, 300mm Radius of Curvature

to nearly steady-state temperature conditions, which will then cause the melt velocity to become more linear. Therefore, any results that do not follow a less-than-linear melt velocity followed by a nearly-linear melt velocity are indicative of numerical error.

Figure 4.6 illustrates this deviation from expected results once again. Full cylinders were mapped against their curved plate counterparts, showing near-agreement between curved plates of different radii of curvature (dashed lines) but slight deviations among full cylinders (solid lines). As these results were not consistent over all geometries of interest, it was clear that there were some numerical issues with applying LT Searight's model to curved surfaces. Therefore, several studies were conducted to analyze meshing methods, ramped coefficients, and error/solution tolerance to allow us to optimize computation time while also creating an accurate, general model.

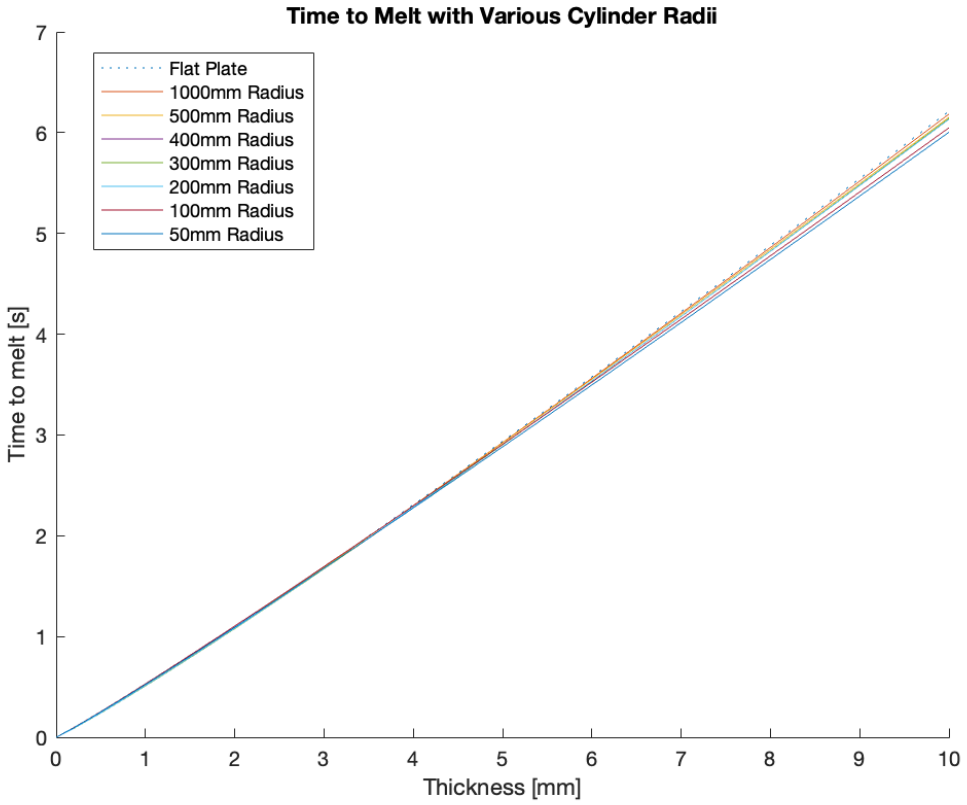

Figure 4.4. Time to Melt through Plates of Various Radii of Curvature over Thicknesses Ranging from 0.1mm to 10mm

4.4 Meshing Analysis

Several methods were studied to optimize computation time versus accuracy. We defined Method 1 as the free triangular meshing method, as shown in Figure 4.7. In this method, COMSOL will establish a mesh of two-dimensional triangles over the surface, which are then "swept into" the structure using Method 1a and Method 1b, ultimately creating layers of triangular prisms. Method 1a will use a mesh 5 layers thick, regardless of structure thickness, while Method 1b will create 2 layers every 1mm of thickness. These methods were chosen to determine if layer thickness affects the results.

At first, we can see from Figure 4.7 that the mesh on the surface of the structure is non-uniform and appears to be non-ideal, as the finer elements are further away from the center.

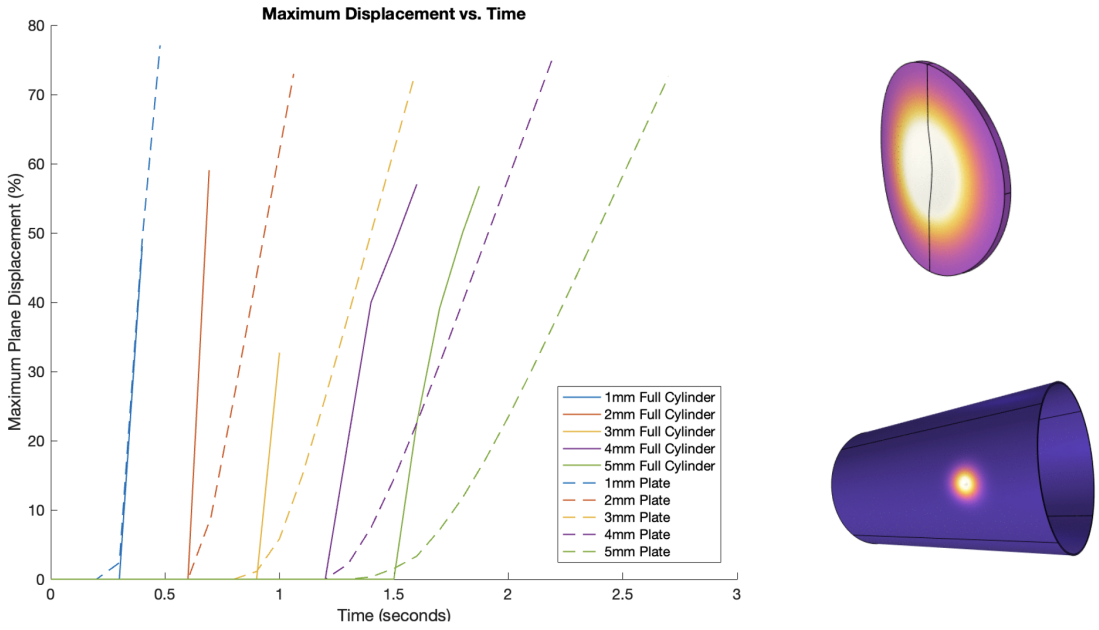

Figure 4.5. Displacement over Time for a 300mm Radius of Curvature Curved Plate and a 300mm Radius Full Cylinder for Various Thicknesses from 1mm to 5mm

This appears at first glance to be problematic, as the temperature gradient effects and mesh velocity will mostly be concentrated in the center.

Method 2 utilized COMSOL's free quad meshing method. This method attempts to fit squares onto the surface, which are once again "swept into" the structure using Method 2a and Method 2b, which have the same attributes as Method 1a and Method 1b. The result of this meshing technique can be seen in Figure 4.8.

This method provides a far less ideal surface than Method 1. Rectangular prisms do not map well to curved surfaces, as we can see from Figure 4.8. The resulting mesh provides far fewer uniform elements on the surface than Method 1 and has the same problems as Method 1 regarding mesh density. Once again, the mesh is less dense in the area of highest dynamics (center of the mesh), and denser near the edges where temperature effects are more negligible, which is a poor optimization for computation time.

The last method for this first study is Method 3, which simply applies a free-tetrahedral mesh

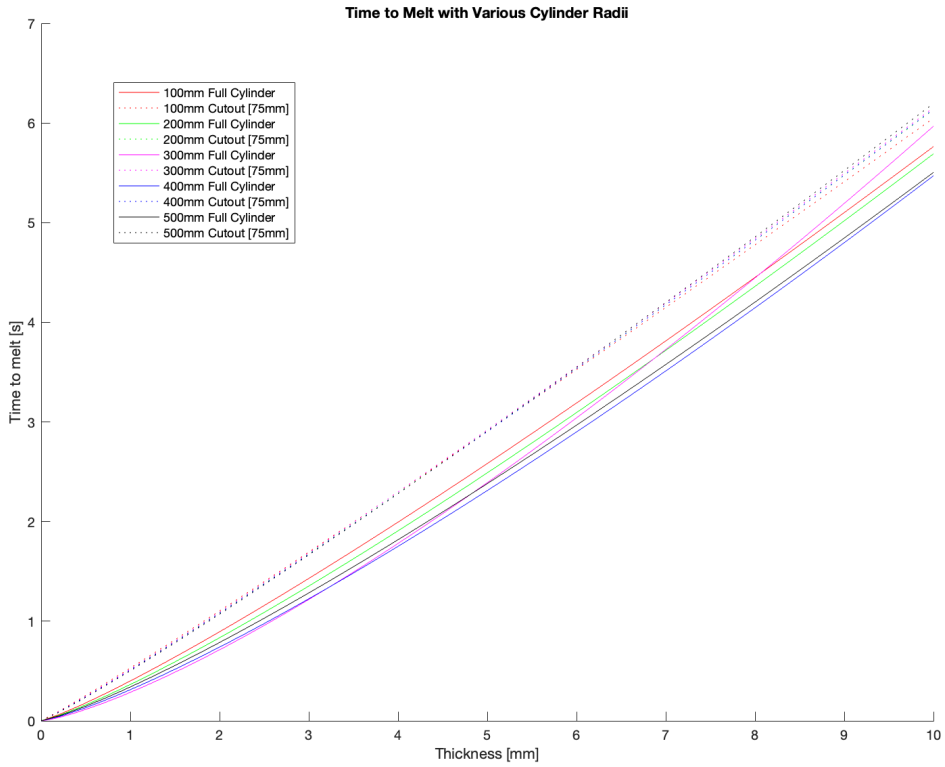

Figure 4.6. Time to Melt through Plates and Cylinders of Various Radii of Curvature over Thicknesses Ranging from 0.1mm to 10mm

to the structure. This method is COMSOL's default meshing method and simply applies tetrahedrons of various sizes and orientations to best map the geometry it is assigned to. The result of this meshing method can be seen in Figure 4.9.

Method 3 does not need to be swept into the structure like Methods 1 and 2, as COMSOL applies three-dimensional tetrahedrons to the structure. As we can see in Figure 4.9, this mesh appears to be much more uniform than Methods 1 and 2 and does not share the same issues with mesh density. As such, the computation times should be far more optimized than the previous methods. Additionally, the end user can apply Method 3 to any geometry, and COMSOL will apply a best-fitting tetrahedral mesh to it. This method will therefore save the user time meshing an imported CAD file and will prevent any computational issues that may be introduced when meeting two meshes of different geometries.

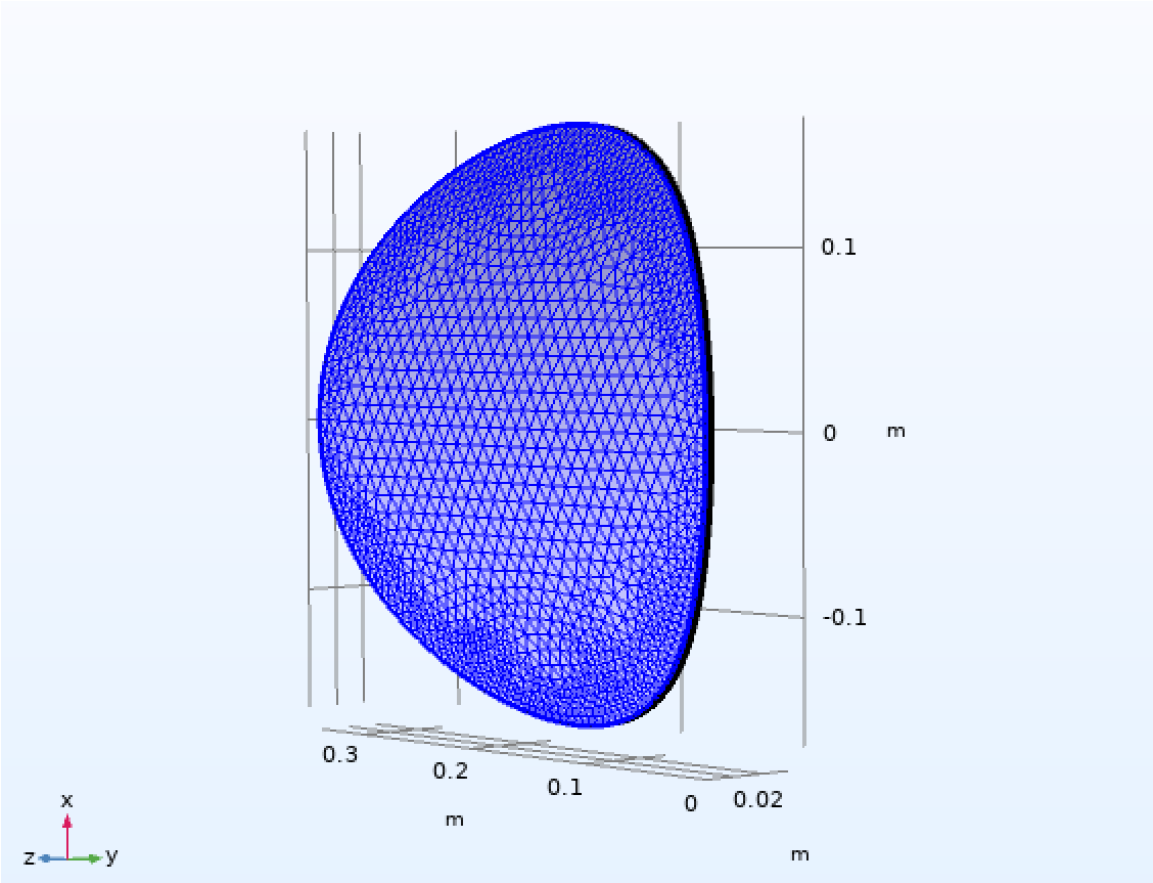

Figure 4.7. Method 1, Free Triangular Mesh

The same laser melting study was performed as before on a plate with a 1000 m radius of curvature, mimicking a flat plate. This was chosen to allow the uniqueness of the meshing methods to still be relevant while also minimizing the numerical error we have seen from previous studies. We observed all mesh displacements over time for each meshing method and determined no significant numerical error was introduced for Methods 1 and 3, as each melt velocity profile matched a less-than linear followed by linear speeds. However, Method 2 showed a lack of smoothness in melt displacement graphs, which shows an introduction of significant numerical error when using this meshing method for this geometry. Ultimately, the results from this study can be illustrated by Figure 4.10.

As shown in Figure 4.10, the method we used to mesh the flat plate seemed to have no significant impact on the accuracy of melt times. However, as computation speed was not

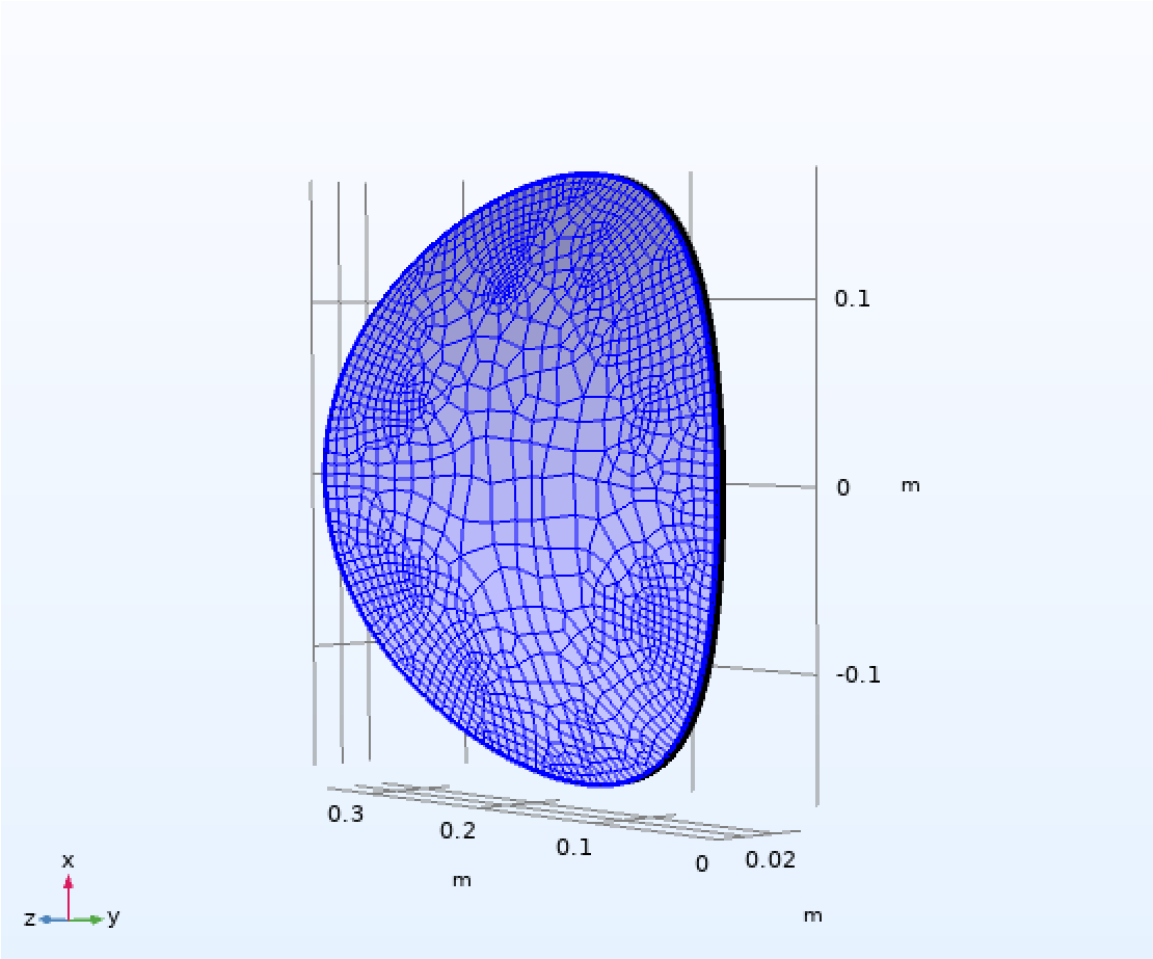

Figure 4.8. Method 2, Free Quad Mesh

optimized for many meshing methods, the time to converge on a solution suffered. The time to compute melt times for 0.1 mm to 10 mm can be seen in Table 4.1. As we can see from Table 4.1 and Figure 4.10, the variable layer thickness increases the computation time by a significant amount, with no change in accuracy.

Additionally, Method 1a offers the fastest computation speed, while Method 3 offers the easiest and fastest mesh setup. This may not be true for all geometries, but the method that the end user chooses to employ will ultimately be decided from the trade-off between setup time and computation time. As imported CAD files can have extraordinarily complex geometries, we use Method 3 for any such study.

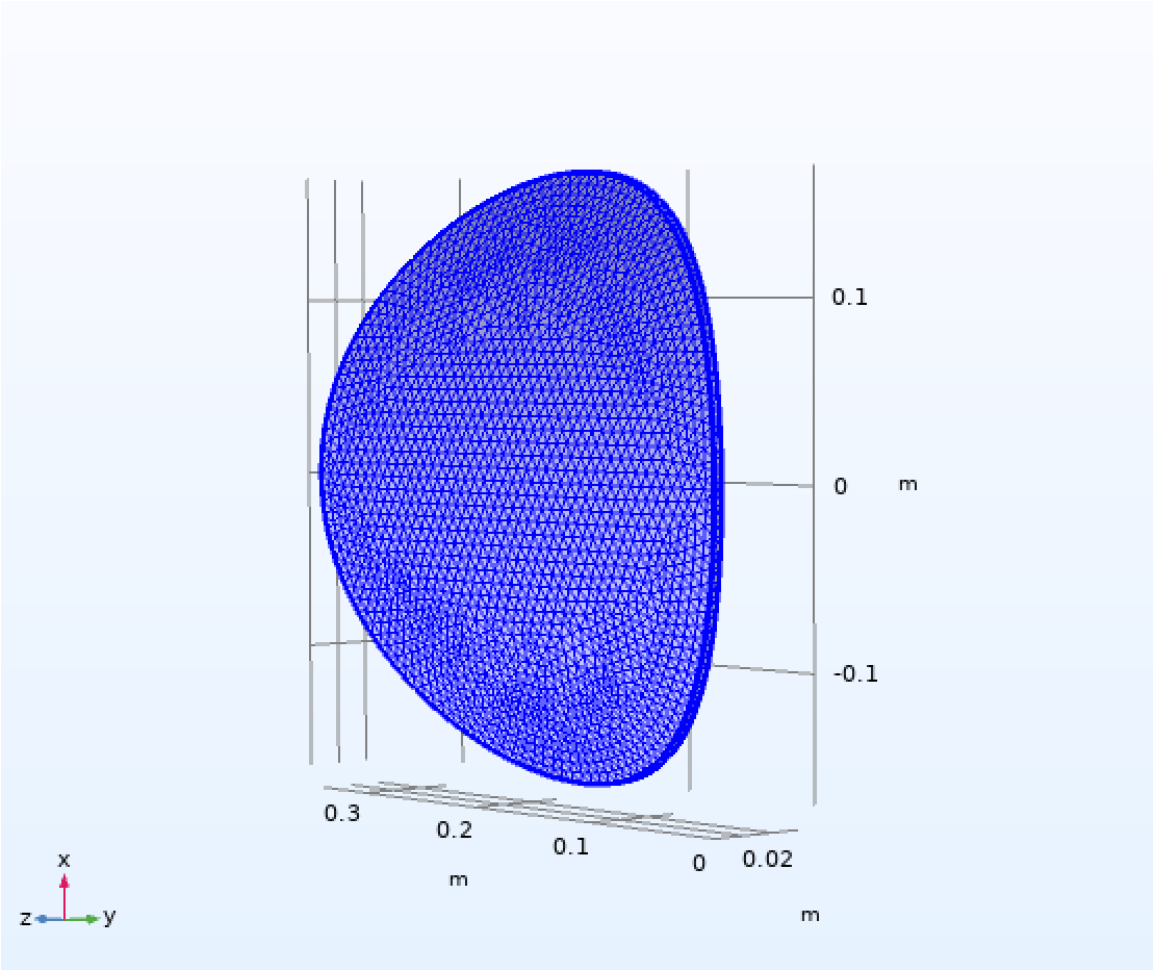

Figure 4.9. Method 3, Free Tetrahedral Mesh

To analyze every aspect that could contribute to numerical error, we then needed to do a detailed study of mesh size on a curved surface. To precisely control mesh size, we introduced a new method called mapped meshing to precisely control mesh size. This method is similar to Method 1 and Method 2 but does not apply the best fit for the geometry on the surface. Instead, a set number of elements are set on one-quarter of the disc, which we will call "Elements Across." Then, COMSOL creates a symmetrical pattern of uniform fit, which can be seen in Figure 4.11.

As we can see from Figure 4.11, this mesh gives a uniform pattern with simple geometry, making it an ideal candidate for this study. This mesh was applied to discs of various sizes,

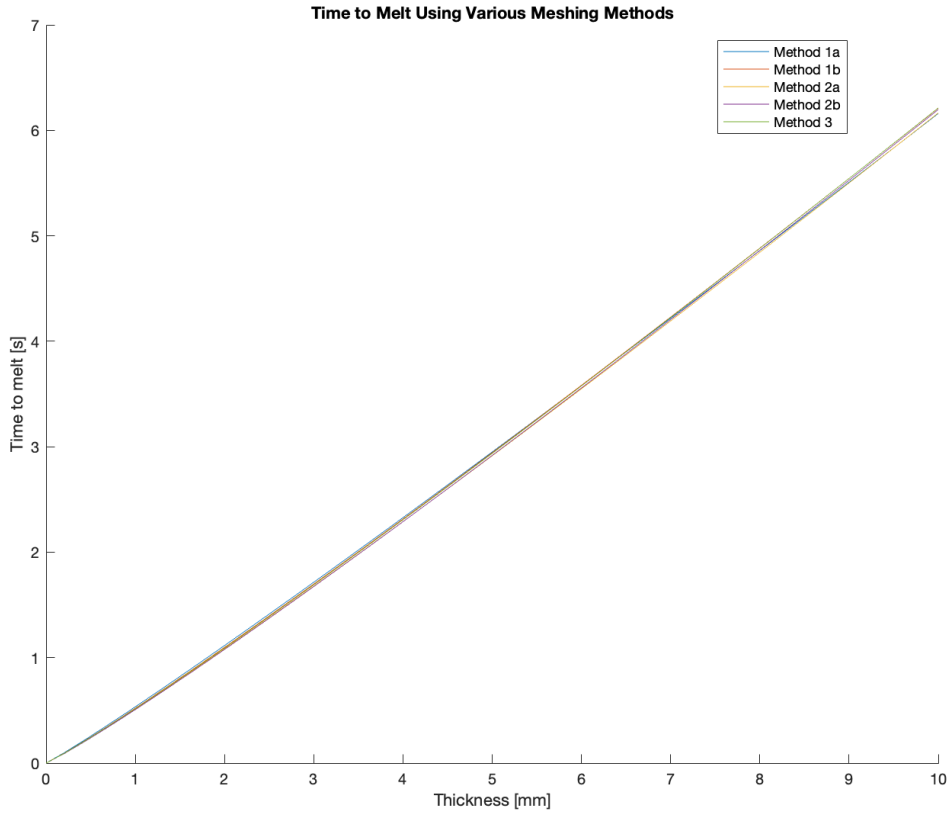

Figure 4.10. Time to Melt using Various Meshing Methods

ranging in radius from 15 cm to 19 cm, each with a radius of curvature of 300 mm. Each mesh was given two layers of elements per disc to minimize computation time; we have previously shown that the number of layers had minimal impact on the accuracy of the results.

Figure 4.12 shows that the results for the smaller-sized disc (15 cm) are relatively independent of mesh element size. The only result where numerical error was significant was when the number of element was set to 25 across. This showed that at least 50 elements across is required to minimize numerical error. The other studies converged on a single melt velocity profile that agreed with the expected results, which was derived from the change in mesh displacement over time.

Table 4.1. Computation Time for Various Meshing Methods

Meshing Method	Time to Compute
Method 1a: Free Triangular, Fixed Element Thickness	11 mins, 25 seconds
Method 1b: Free Triangular, Variable Element Thickness	39 mins, 29 seconds
Method 2a: Free Quad, Fixed Element Thickness	14 mins, 55 seconds
Method 2b: Free Quad, Variable Element Thickness	1 hr, 1 min, 3 seconds
Method 3: Free Tetrahedral	15 mins, 15 seconds

Moving to the 19 cm disc in Figure 4.13, we began to see a trend where only higher fidelity models resulted in a melt velocity profile that was not affected by numerical error. As element fidelity increased beyond 100 elements across—that is to say, 100 elements along one quarter of the modeled disc—we saw that all melt velocity profiles converged to expected results. It should be noted that these higher fidelity models drastically increased computation time. Whereas the 25 element across took approximately eight minutes, the 250 element across model took approximately one hour, 12 minutes.

Many discs of other sizes were studied, but we will inspect the final set of results for brevity. Figure 4.14 illustrates the results from the largest disc studied and shows an important trend we will need to consider moving forward. The lower-fidelity mesh models used on the larger disc deviated from each other a fair amount. In contrast, the higher-fidelity mesh models converged to a single result starting around 175 elements across. However, no results were free of numerical error, and even the results that converged did not match expected melt velocity.

The trends we can take away from these three studies are as follows:

- Larger geometries are more prone to numerical error.
- Larger element sizes are more prone to numerical error.
- Larger element sizes are less likely to converge on an accurate result.

Knowing this, we can consider a set of rules that will reduce numerical error and provide the most accurate results. Next, we will consider the ramped parameter's role in this goal.

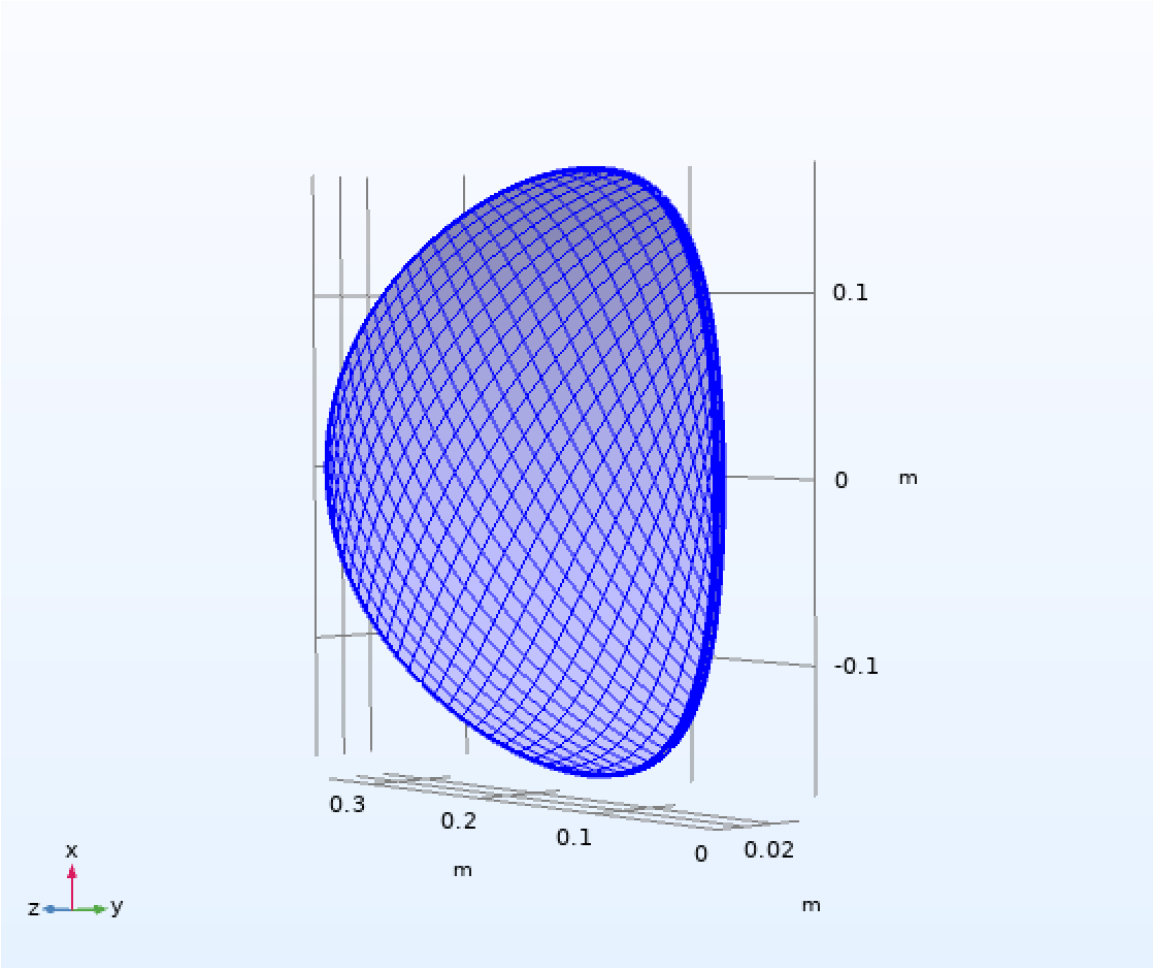

Figure 4.11. Mapped Meshing Method

4.5 Ramped Coefficient Analysis

In order to analyze a large number of samples in a timely manner, we will first examine a disc with a 17 cm radius and a mapped mesh with 175 elements across. As we saw in the previous section, a mapped mesh with 175 elements across is where we began to see convergence in all cases. Additionally, by using a smaller disc size, we can begin to quickly formulate trends for how different ramped coefficients affect melt times. As a reminder, the ramped coefficient determines how quickly the energy is removed from the surface of the disc via the fictitious ablative flux. Let us first analyze this sample across a range of ramped coefficients and determine how laser power might affect these results. Figures 4.15, 4.16, and 4.17 display the melt profiles for a 17 cm radius plate irradiated by beams of 5 cm width

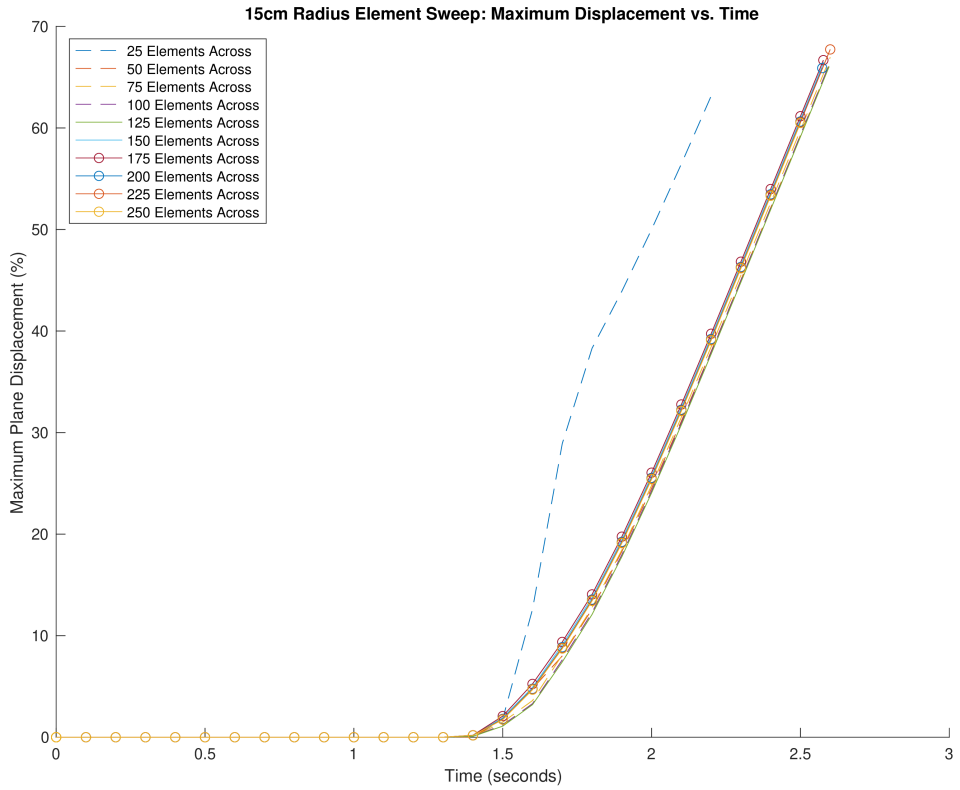

Figure 4.12. Displacement vs. Time for Mapped Mesh on a Curved Disc with Radius of 15cm and a Radius of Curvature of 300mm

for 50 KW, 100 KW, and 200 KW, respectively.

Figure 4.15 begins to illustrate how changing the ramped coefficient will affect melt times. Of all the ramped coefficients shown, 2E4 is the only one that appears to be free of numerical error, based on the less-than-linear, linear melt times we demonstrated with a flat plate. Interestingly, the 4E4 case shows a large amount of error when melting begins, even demonstrating that the mesh underwent negative velocities at some point in time. This should not be possible, as melting occurs only in one direction and only when the temperature reaches a certain point. It is not known the exact reason why this occurred in this instance, but we know for certain that is indicative of numerical error.

In the cases of the 100 KW and 200 KW beams in Figures 4.16 and 4.17, respectively,

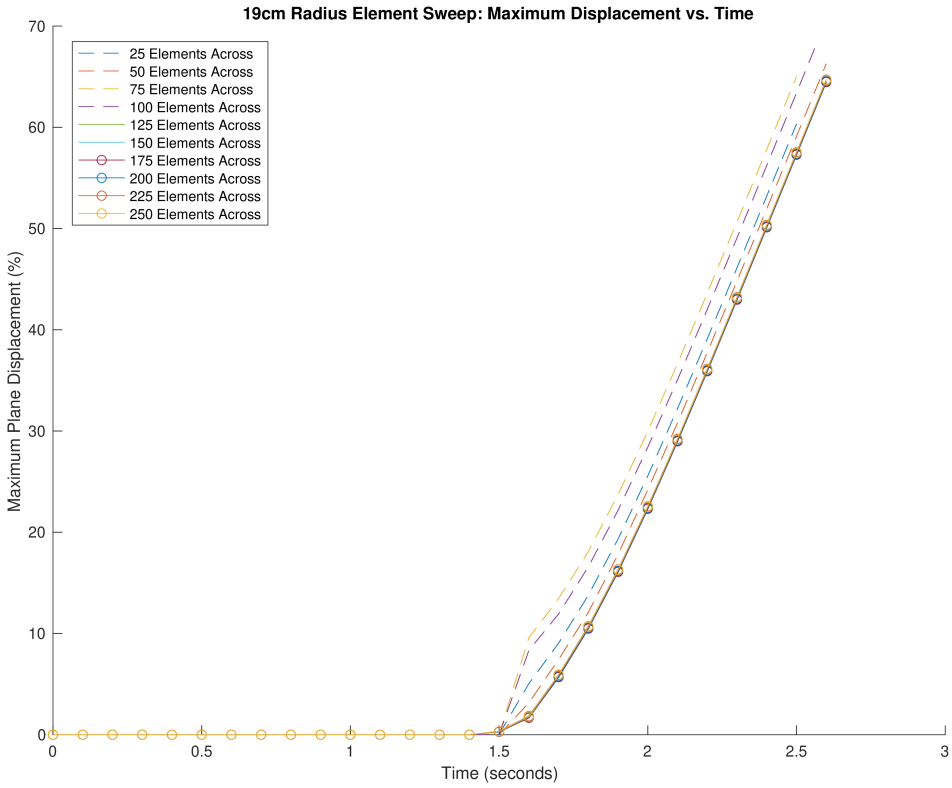

Figure 4.13. Displacement vs. Time for Mapped Mesh on a Curved Disc with Radius of 19cm and a Radius of Curvature of 300mm

we see once again the instances where numerical error is introduced in the system in the transient state. One trend in these higher power studies is that a higher ramped parameter is required for melting simulations to converge. The ramped parameter ultimately determines the strength of the fictitious heat flux that corrects melt temperature; therefore, to avoid an excess in temperature that corresponds to an erroneously high melt velocity, a high ramped parameter is required to correct the temperature profile to steady-state in the shortest time possible. Additionally, the melting profiles appear to have more continuous slopes, likely due to the smaller time steps performed for this study—we will discuss this further in the next section.

One key trend can be taken away from all of these instances, even those with some form of

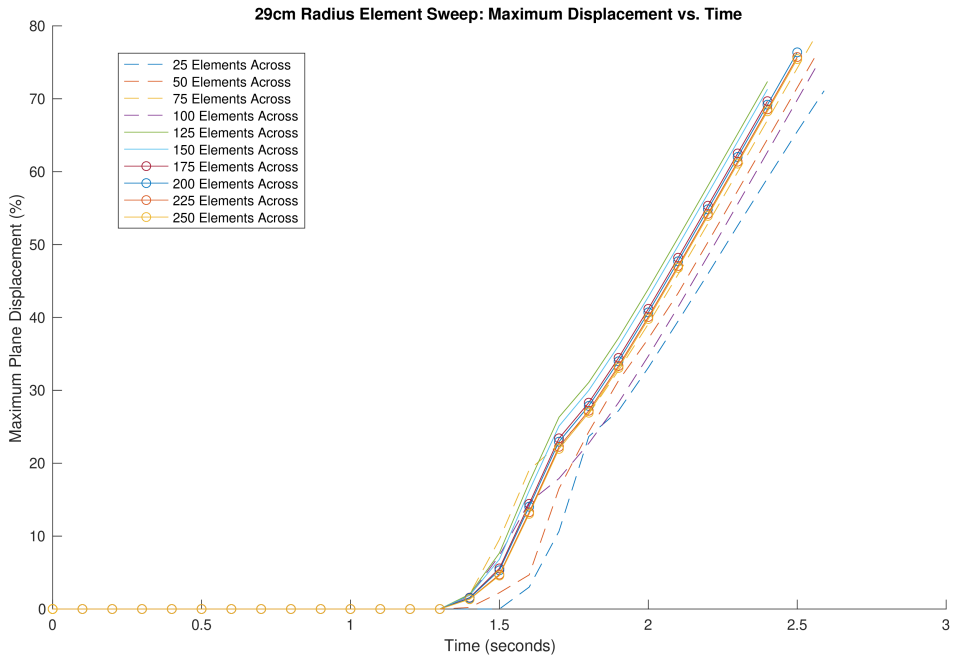

Figure 4.14. Displacement vs. Time for Mapped Mesh on a Curved Disc with Radius of 29 cm and a Radius of Curvature of 300mm

numerical error: every melt profile's steady-state melt velocity is the same. This informs us that the numerical error only significantly changes the melt evolution in the transient state when melting first begins.

We can think of the ramped parameter as a damping function. If the ramped parameter is too low, the temperature will take too long to find a steady-state value—this case is similar to an over-damped oscillator. If the ramped parameter is too high, the temperature will oscillate wildly before reaching a steady-state value—this case is similar to an under-damped oscillator. Recall that the magnitude of mesh velocity is directly dependent on the difference between the modeled temperature and the melt temperature. Therefore, the numerical error induced in the system by ramped parameters will ultimately be due to the variation in melt velocity in the transient state.

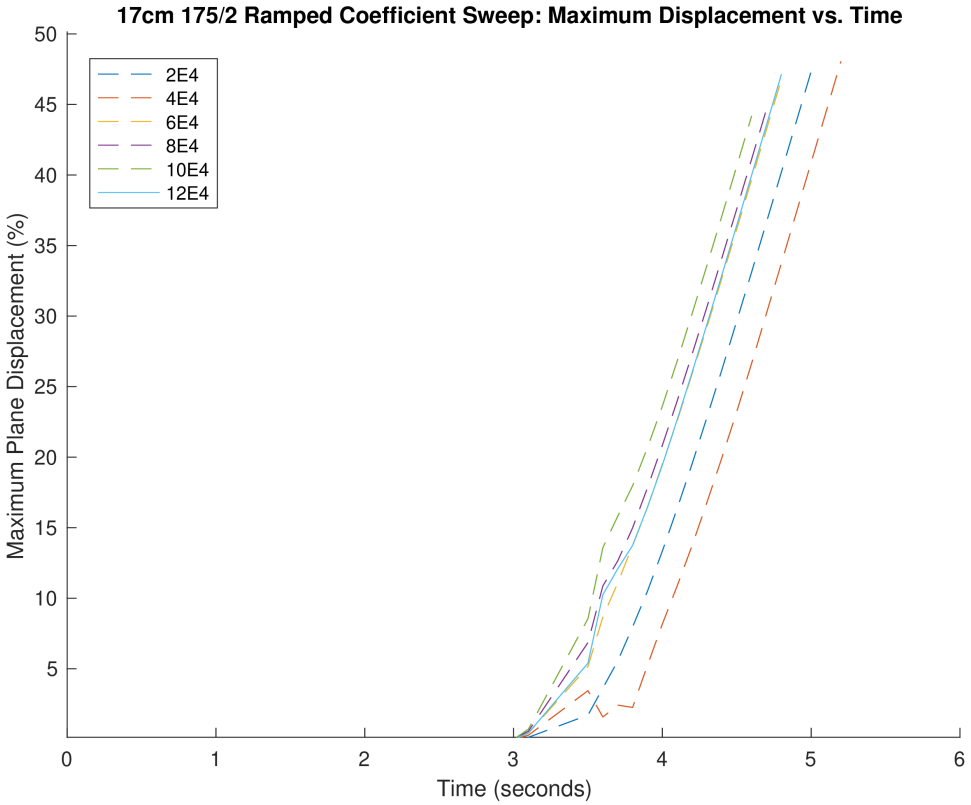

Figure 4.15. Displacement vs. Time of Various Ramped Coefficients for Mapped Mesh of 175 Elements across and 2 Thick on a Curved Disc with a Radius of 17 cm and a Radius of Curvature of 300mm for a 50 KW beam over a 5cm Spot Size

4.6 Error Tolerance Analysis

If we continue the analogy of the damped oscillator, we can then consider that as smaller time steps are performed to calculate each next instance of melting, less error is introduced into the system. If the discrete instances of melting become near-continuous, then the magntitude of the ramped coefficient matters less. This is because every system has a steady-state melt velocity, where the total amount of energy introduced to each element is the same amount of energy dissipated by ablation. Imagine a case where the time step is very long. Suppose the temperature deviates from this steady state value. In that case, the damping coefficient must be very specific to allow the temperature to quickly correct

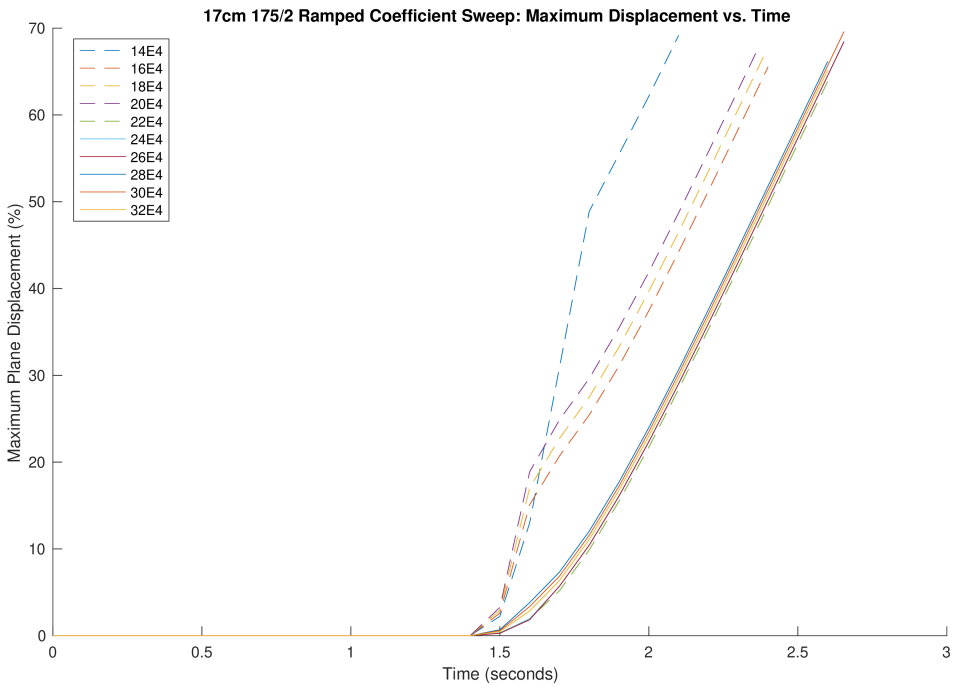

Figure 4.16. Displacement vs. Time of Various Ramped Coefficients for Mapped Mesh of 175 Elements across and 2 Thick on a Curved Disc with a Radius of 17 cm and a Radius of Curvature of 300mm for a 100 KW beam over a 5cm Spot Size

itself and minimize melt velocity error. Compare this case to one where the time step is near-continuous. Even if the damping coefficient strays from the "critical" value, there will be more calculations to correct this error in less time. By forcing this time step to be smaller and lowering the overall error tolerance of the system, the result will be a melt profile with minimal error. COMSOL controls both of these values through an error tolerance variable, which determines the value that two iterations of the Newton-Raphson method must agree upon. It should be noted that computation times become much larger by creating a tighter tolerance. Therefore, creating an accurate melting simulation will be a fine balance between picking optimum values for the mesh size, ramped coefficient, and error tolerance.

Error tolerance has a clear effect as the surface deviates from a flat plate to a curved surface. Until now, all simulation results shown have used COMSOL's default error tolerance value

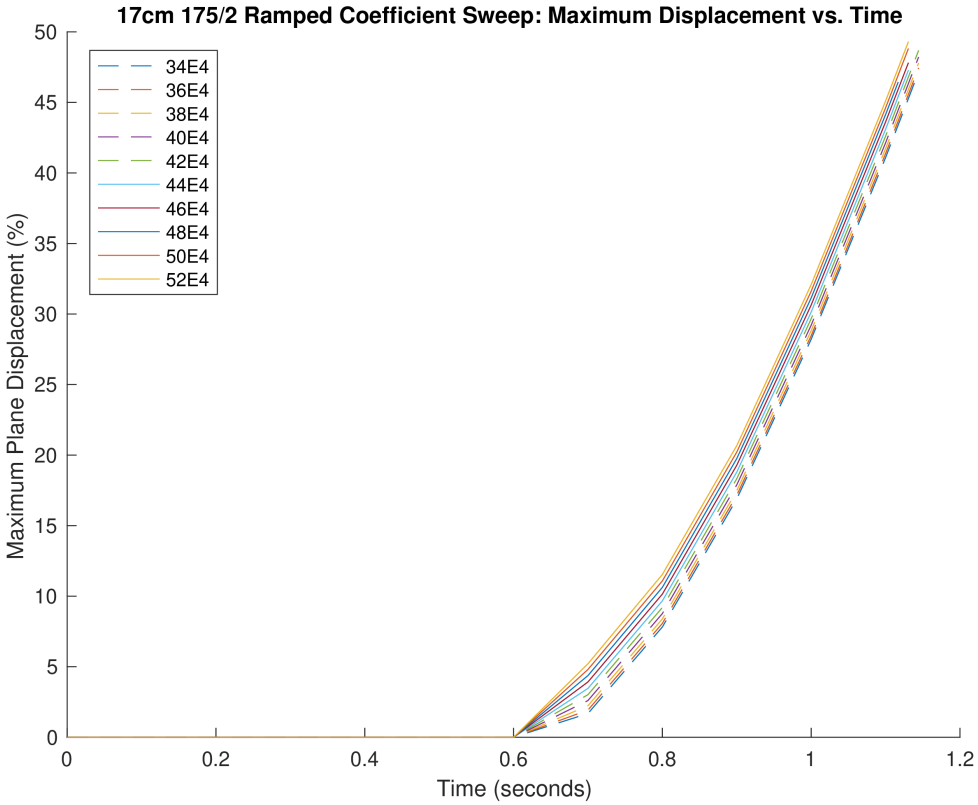

Figure 4.17. Displacement vs. Time of Various Ramped Coefficients for Mapped Mesh of 175 Elements across and 2 Thick on a Curved Disc with a Radius of 17 cm and a Radius of Curvature of 300mm for a 200 KW beam over a 5cm Spot Size

of 0.01. To illustrate how much of an effect error tolerance, and thus time steps, have on melt velocities, let us consider the data represented in Figure 4.18 and Figure 4.19.

Figure 4.18 clearly illustrates how the melt profile changes drastically as we deviate from a flat plate, given a less-restrictive error tolerance of 0.1. Although this is a less-restrictive tolerance than used in this study, it is purely meant to illustrate how much of an effect such a parameter has on melt profile accuracy. At some radii, we even see melting begin nearly half a second quicker than we would expect. However, as seen in Figure 4.19, we can see extraordinary results by tightening the tolerance to .001. As expected, the curved discs of any radius closely resemble the melt profile of a flat disc—all of which are relatively free

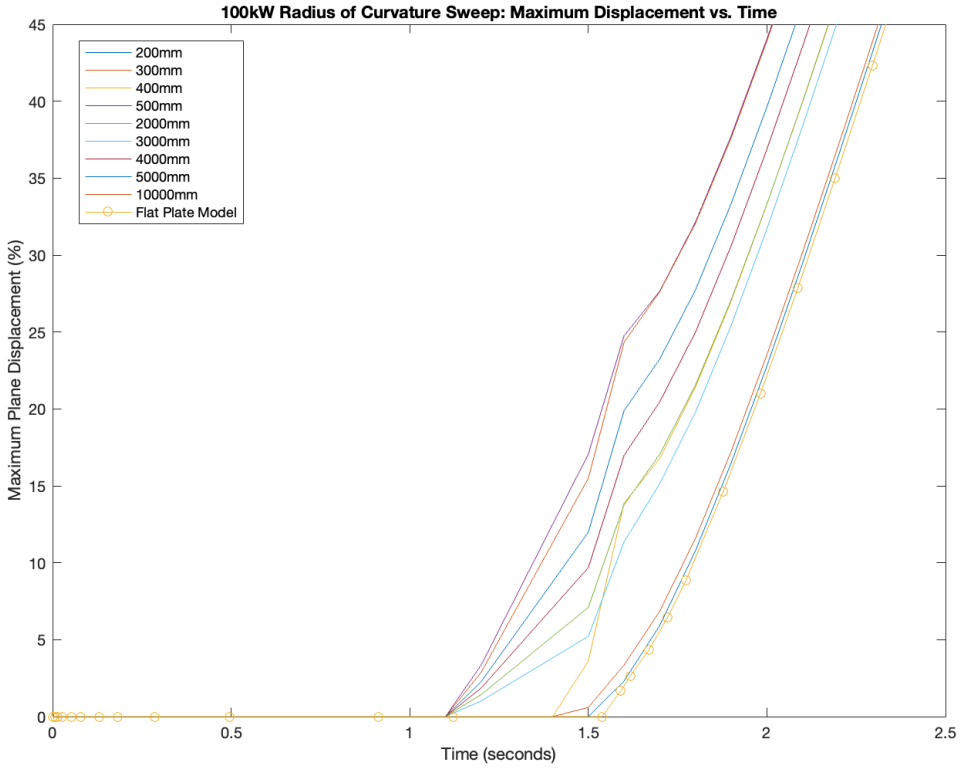

Figure 4.18. Displacement vs. Time of Various Radii for Error Tolerance of 0.1

of error.

This result is promising, and shows the effect time steps and error tolerance has on these simulations. Though tighter tolerances increase computation time, they vastly increase melt profile consistency and remove a large amount of numerical error from the transient melting instances. It is worth considering how much of an effect and even tighter tolerance will have on our simulations.

Let us consider two cases for ramped coefficient sweeps: one with a tolerance of 1E-3 and one with a tolerance of 1E-6. Comparing figures 4.20 and 4.21 to Figure 4.16 clearly illustrates how a tighter error tolerance allows for a greater range of ramped coefficients to be used while still achieving accurate melt profiles. Moving from the default error tolerance

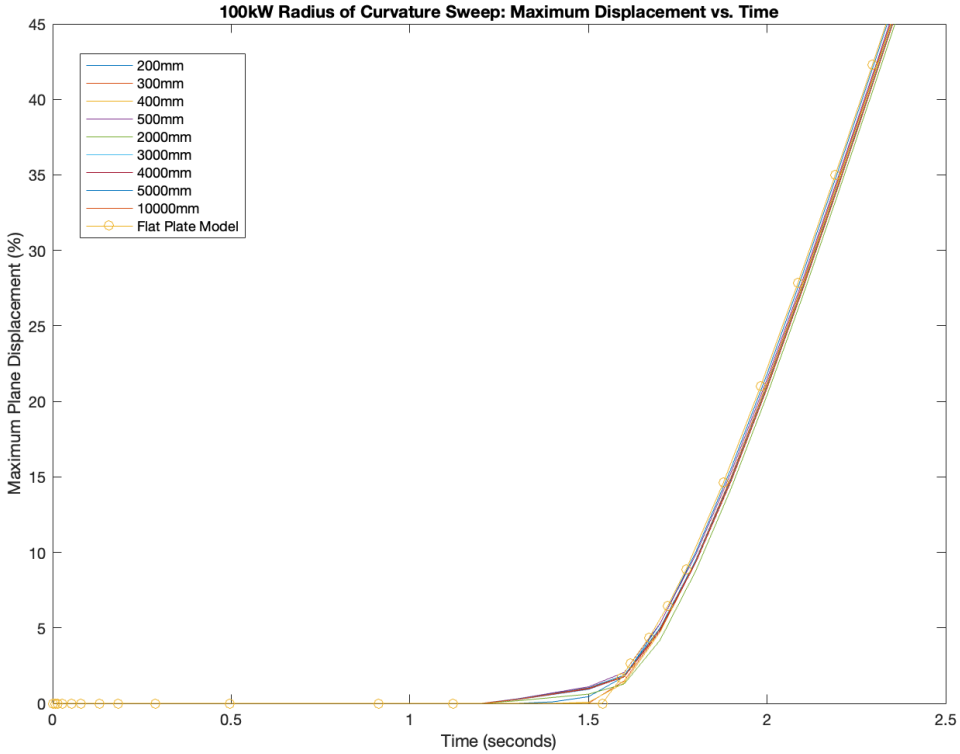

Figure 4.19. Displacement vs.Time of Various Radii for Error Tolerance of 0.001

of 1E-2 to 1E-3 alone makes the wide range of ramped coefficients tested relatively error-free. The only deviation between ramped parameters is how the material behaves when melting begins, with all but the lowest ramped coefficient resulting in parallel melt profiles. However, there are minute deviations between the melt profiles even as ramped coefficients increase in the case of an error tolerance of 1E-3.

Tightening the error tolerance to 1E-6 causes the lower ramped coefficients to converge on a single result, with every tested ramped parameter resulting in parallel melt profiles. This suggests once again that steady-state melt velocities are independent of ramped coefficient. We can determine from Figure 4.21 that higher ramped coefficients are preferable to achieve an accurate result. Lower ramped coefficients do not "correct" the temperature adequately, even if lower time steps and error tolerances are implemented. We will use an error tolerance

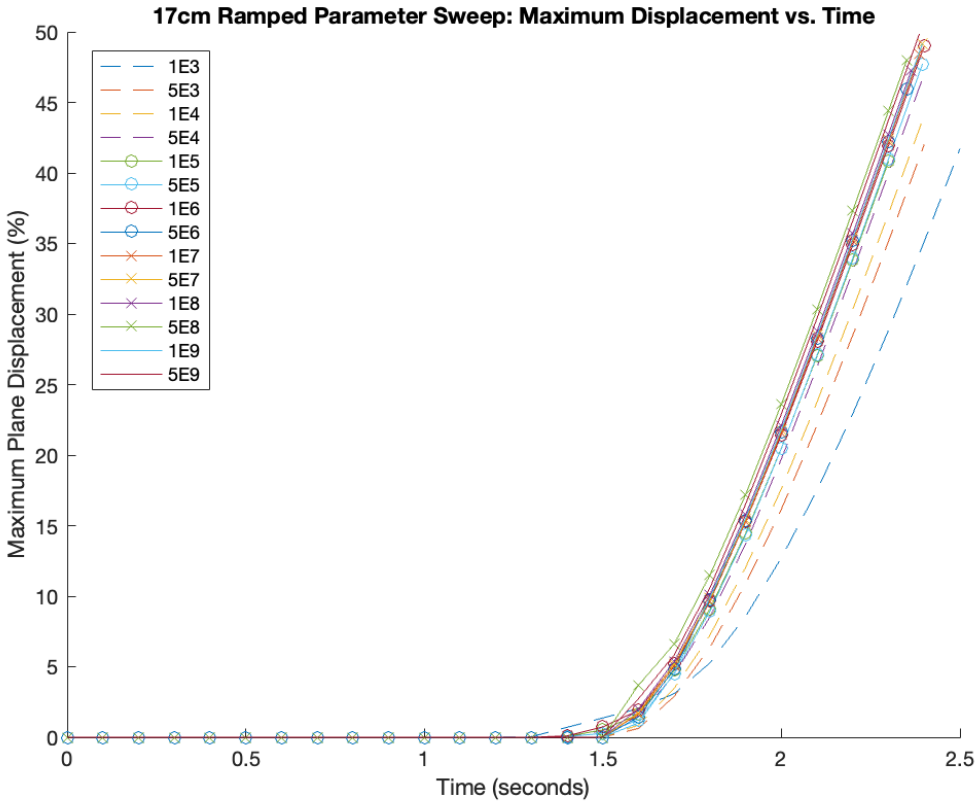

Figure 4.20. Displacement vs.Time of Various Ramped Coefficients for Error Tolerance of 1E-3

of 1E-6 and a relatively high ramped coefficient, determined by iterative testing, to guarantee numerically consistant results for future studies.

4.7 CAD Example

Now that we have established a series of parameters contributing to numerical error, we can import a CAD model and compare its melt profile to previously established geometries: a flat plate and a curved disc. We will also examine a 29 cm "cutout" of the missile to compare computation times and melt profile accuracy. For this study, we will use the common parameters of a 1E-3 error tolerance, a thickness of 4 mm, 100 KW beam power, and a 5 cm spot size. Additionally, the radius of curvature for this fictitious missile is 75 cm,

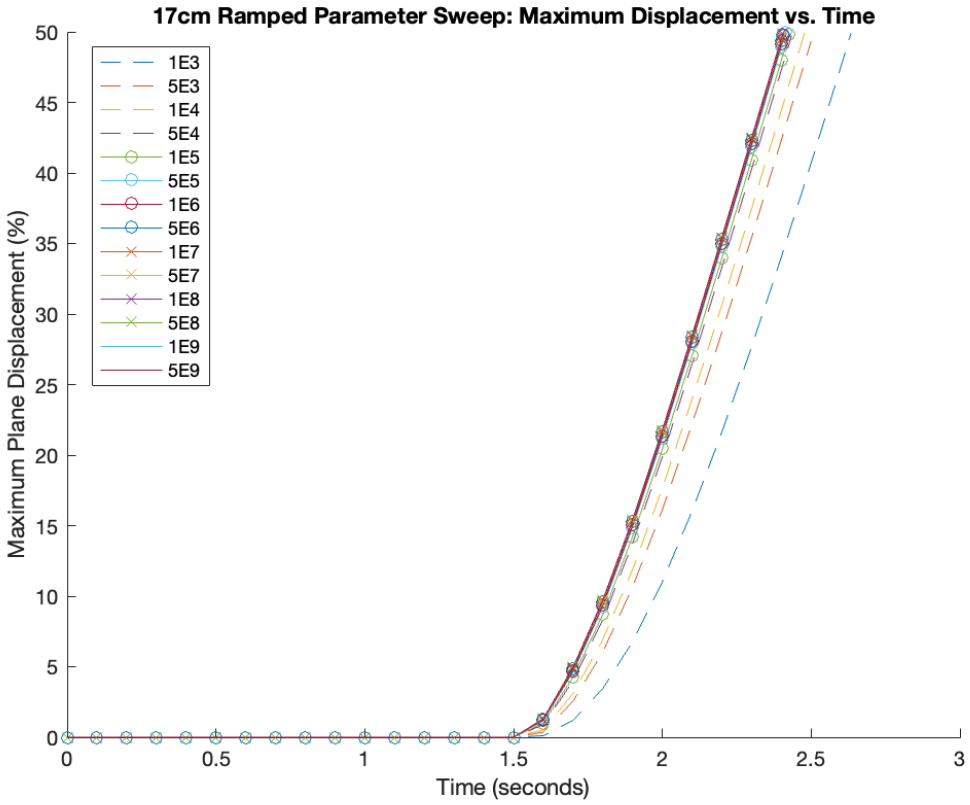

Figure 4.21. Displacement vs.Time of Various Ramped Coefficients for Error Tolerance of 1E-6

so we will continue to use that radius of curvature for the curved disc.

Figure 4.22 illustrates that there are minimal differences in the melt profiles of these geometries. We can show, therefore, that the choice in geometry modeled is dependent on what the user wishes to study. Since the melt profiles of the curved plate and the flat disc converge, it is evident that the radius of curvature does not appear to have any significant effect. Thus, if a rough calculation for melt time is desired, a flat plate with a similar thickness as its representative target can suffice as a stand-in.

Most importantly, however, we can determine from these melt profiles that the method developed for simulating the melting of a complex CAD geometry closely matches representative geometries. Additionally, the values predicted by this model are close to the values

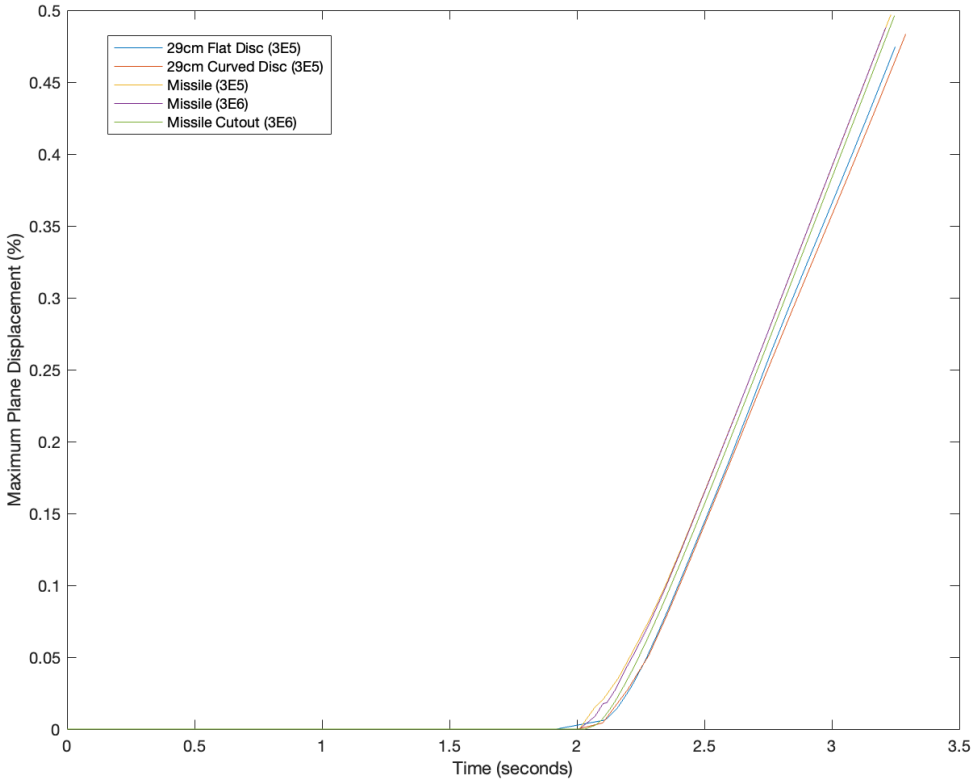

Figure 4.22. AE: Displacement vs.Time of Various Geometries

predicted by first principles equations. Equation 3.12 predicts a melt time of approximately 4.5 seconds, and by extrapolating the graphs from Figure 4.22, we can predict a melt time of 4.3 seconds. We can see that this model gives reasonable results and free of numerical error, thus making it suitable as a basis for future lethality analyses. Therefore, physics simulations can be performed on this CAD that would not be possible in simple geometries, such as changes to aerodynamics, thermally induced stresses, and convective losses.

Finally, Figure 4.23 illustrates the CAD of the missile laser for the data obtained in Figure 4.22. This graphic shows the heat profile of the missile at 50% melt-through and the displacement of the structure where lased. This method makes it fairly straightforward to import a developed CAD file and apply rigorous physics simulations.

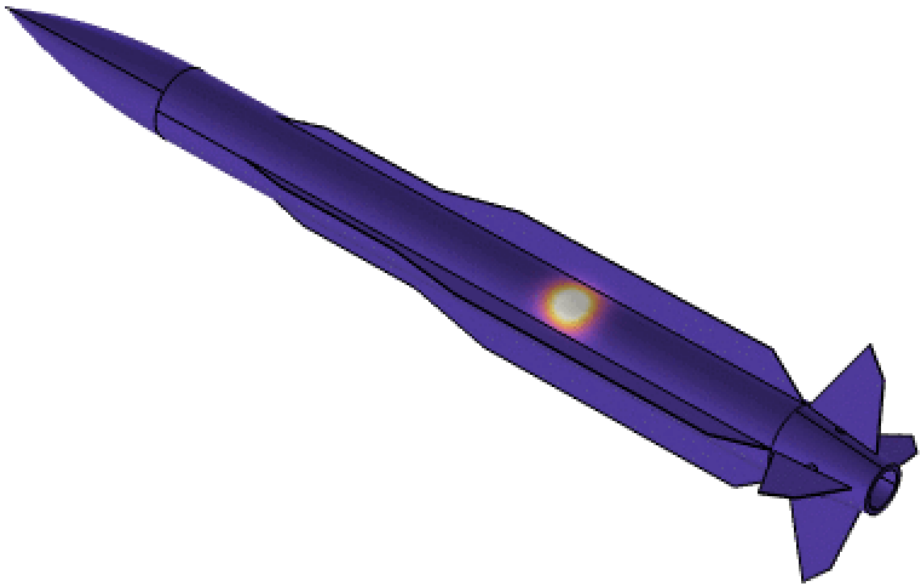

Figure 4.23. Heat and Displacement Profile of Lased Missile

THIS PAGE INTENTIONALLY LEFT BLANK

CHAPTER 5:
Conclusion

5.1 Melting Method

The simulations reported on in Chapter 4 allow us to generate a method to optimize computation time and accuracy. In this section, we will provide several recommendations to the end user. Once the model is set up and a CAD file has been imported and prepared, the user is recommended to mesh with auto-tetrahedral with a "finer" resolution. As seen in Figure 4.10, the shape of the mesh does not significantly affect melting accuracy, and the simplistic approach of auto-tetrahedral meshing allows for experiments to be run with a simpler setup. However, if computation time must be optimized, it was observed that free-triangular swept with a constant two-element thickness produced the fastest results. It is worth noting that this setup may take more time and require the user to have more advanced knowledge of local mesh quality in COMSOL.

With a meshed object in COMSOL, it is recommended to run a "zeroing" study before performing any further experiments. This study should consist of a ramped parameter sweep in any number of intervals from 1E3 to 1E9 with an error tolerance of 1E-3, with a beam directly incident on the target. After analyzing the data from this sweep, it is recommended to use the lowest ramped parameter that causes the melt profiles to converge. For the actual study the user wishes to perform, an error tolerance of 1E-3 can be used for speed, but a 1E-6 error tolerance will guarantee more accurate results. It is not recommended to use any values greater than 1E-3, as numerical error becomes prominent for any curved surfaces.

It should be noted that a full CAD is not recommended for simple melt calculations, as a flat disc will provide the same accuracy for melt times at a fraction of the computation time. A full CAD melt should only be utilized if the experiment cannot be performed by melting a disc, such as by observing stresses, aerodynamic effects, or effects unique to a missile geometry or beam orientation.

5.2 Future Work

The immediate follow-up work for this model should include radiation losses. This loss was ignored for this work but will be relevant for materials with lower thermal conductivity and higher emissivity. Additionally, aerodynamic effects should be incorporated so that convective losses can also be considered. For a mid-flight threat, one can estimate that airflow will act as an effective coolant, thus increasing melt time. By incorporating aerodynamic effects, one can also study how turbulent boundaries adjust once threat geometry is adjusted; it is expected that localized turbulent flow at the melt site could cause alternative kill conditions. Finally, stresses on the missile should also be incorporated into this model. At a minimum, one should consider thermal stresses and aerodynamically induced stresses. Observing the threat's materials approach yield stress can determine the most vulnerable times of flight and lasing locations for specific threats. A full melt-through of the target may not be required for a kill—reducing dwell times for the direct energy weapon and allowing it to engage more threats in the same period of time.

List of References

[1] M. Searight, "Directed energy lethality and engagement modeling," Master's thesis, Naval Postgraduate School, 1 University Circle, Monterey, CA 93943, June 2022.

[2] C. R. Services, "Navy shipboard lasers: Background and issues for congress," December 2022.

[3] Lockheed Martin. (2021, January). [Online]. Available: https://www.lockheedmartin.com/en-us/news/features/2021/more-than-a-laser-helios-is-an-integrated-weapon-system.html

[4] D. P. M. Captain David Hart, "Slide 5 from briefing on ddg(x) program," presented at Surface Navy Association annual symposium, January 2022.

[5] J. Blau, "Notes for ph4858: Directed energy weapons, dept. of physics, Naval Postgraduate School, Monterey, CA, USA, May 2023, quarter 1," October 2022.

[6] DJI. (2023, January). [Online]. Available: https://www.dji.com/phantom-4-pro-v2

[7] A. Papadogiannis, N. Papadogianni, A. Carabelas, S. Tsitomeneas, P. Kyraggelos, and T. Chondros, "The mirror weapon in archimedes era," in *Proceedings of EUCOMES 08*, M. Ceccarelli, Ed. Dordrecht: Springer Netherlands, 2009, pp. 29–36.

[8] J. Hecht, "Half a century of laser weapons," *Opt. Photon. News*, vol. 20, no. 2, pp. 14–21, Feb 2009. Available: https://www.optica-opn.org/abstract.cfm?URI=opn-20-2-14

[9] New York Times. (2022, May). [Online]. Available: https://www.nytimes.com/2022/05/05/us/politics/moskva-russia-ship-ukraine-us.html

[10] Baykar. (2023, January). [Online]. Available: https://www.baykartech.com/en/uav/bayraktar-tb2/#:~:text=Bayraktar%20TB2%20is%20a%20Medium,ISR)%20and%20armed%20attack%20missions.

[11] ENVIR215. (2005, 03). [Online]. Available: https://www.ocean.washington.edu/courses/envir215/energynumbers.pdf

[12] USNI. (2018, July). [Online]. Available: https://www.usni.org/magazines/proceedings/2018/july/reload-missile-shooters-sea

[13] Naval History and Heritage Command. (2018, August). [Online]. Available: https://www.history.navy.mil/content/history/nhhc/get-involved/essay-contest/2017-winners/additional-essay-contest-submissions/a-century-of-replenishment-at-the-sea.html

[14] Corning. (2023, January). [Online]. Available: https://www.corning.com/worldwide/en/products/advanced-optics/product-materials/aerospace-defense/missile-domes-radomes.html

[15] U. P. F. P. A. Commander, ""USS Portland conducts laser weapon system demonstrator test," May 2020.

[16] J. Hohlfeld, S.-S. Wellershoff, J. Güdde, U. Conrad, V. Jähnke, and E. Matthias, "Electron and lattice dynamics following optical excitation of metals," *Chemical Physics*, vol. 251, no. 1, pp. 237–258, 2000. Available: https://www.sciencedirect.com/science/article/pii/S0301010499003304

[17] R. S. John R. Howell, M. Pinar Menguc, *Thermal Radiation Heat Transfer*, 6th ed. CRC Press, September 2015.

[18] ChemistryTalk. (2023, January). [Online]. Available: https://chemistrytalk.org/heat-of-fusion/

Initial Distribution List

1. Defense Technical Information Center
   Fort Belvoir, Virginia
2. Dudley Knox Library
   Naval Postgraduate School Monterey,
   California